Technical Report
1245

Digital Tracker Array Radiation Test Report

D.K. Fischi
S.L. Riccardi
J.R. Wey
A.F. Kryzak
T.D. Gardner
K.A. McIntosh
S. Lee
M.H. Blackwell

20 January 2021

Lincoln Laboratory
MASSACHUSETTS INSTITUTE OF TECHNOLOGY
LEXINGTON, MASSACHUSETTS

This material is based upon work supported under Air Force Contract No. FA8702-15-D-0001.

This report is the result of studies performed at Lincoln Laboratory, a federally funded research and development center operated by Massachusetts Institute of Technology. This material is based upon work supported under Air Force Contract No. FA8702-15-D-0001. Any opinions, findings, conclusions or recommendations expressed in this material are those of the author(s) and do not necessarily reflect the views of the U.S. Air Force.

Massachusetts Institute of Technology
Lincoln Laboratory

Digital Tracker Array Radiation Test Report

D.K. Fischi
Group 97

S.L. Riccardi
J.R. Wey
A.F. Kryzak
T.D. Gardner
K.A. McIntosh
S. Lee
Group 87

M.H. Blackwell
Group 48

Technical Report 1245

20 January 2021

Lexington Massachusetts

UNCLASSIFIED

This page intentionally left blank.

CONTENTS

LIST OF ILLUSTRATIONS

LIST OF TABLES

This page intentionally left blank.

1. INTRODUCTION

A requirement of all space programs is to determine to what degree susceptibility to the space radiation environment will present a risk to the mission. The process of this determination and subsequent mitigation, if needed, is called radiation hardness assurance (RHA). The process is outlined in Figure 1.

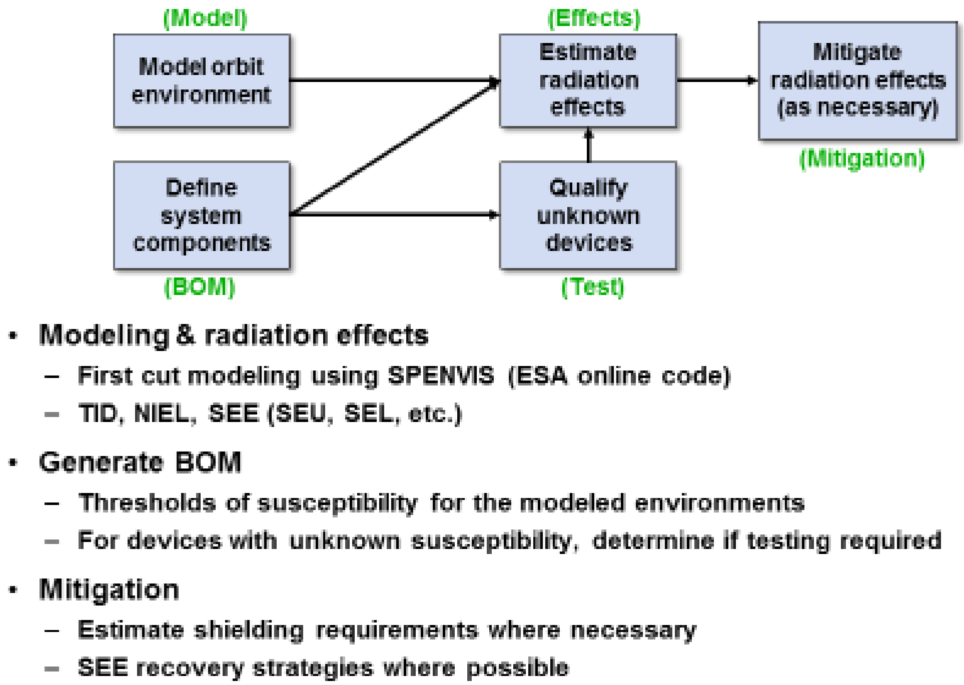

*Figure 1. Radiation hardness assurance process. *Acronyms: Bill of Materials (BOM); SPace ENVironment Information System (SPENVIS); European Space Agency (ESA); Total ionizing dose (TID); Non-ionizing energy loss (NIEL); Single-event effect (SEE); Single-event upset (SEU); Single-event latch-up (SEL).*

For the Digital Tracker Array (DTA) program, there were some unique concerns and constraints, which needed to be addressed. The primary component of this design was a hybrid sensor based on the Massachusetts Institute of Technology Lincoln Laboratory (MIT LL) Digital-pixel Focal Plane Array (DFPA) which was bump-bonded to InGaAs short wave band infrared detectors. Though used successfully in ground experiments, its space capability was an open question. In particular, the CMOS-based design and its susceptibility to radiation was unknown. Further, because the design of the package was extremely size, weight, and power constrained, radiation mitigation could become a problem (BISA, Belgian Institute for Space Aeronomy, 2019).

A test campaign was planned which consisted of several decision gates. The first gate was the total ionizing dose (TID) resistance of the DFPA transistor processes. This was an easy test as Lincoln Laboratory had the facility to irradiate transistor test structures with an Aracor x-ray machine. If the TID failure level was low, there would be no point moving on to more expensive tests, in terms of both time and cost. The second gate was to test for single event latch-up (SEL). This was a more time consuming test, but simple in terms of evaluating. The concern was that CMOS structures are susceptible to latch-up, so if the linear energy transfer (LET) level was too low, the mitigation would be difficult. Finally, the devices were tested for single-event functional interrupts (SEFI) which require a reset to recover. Once again, if the LET levels were too low, mitigation would be difficult.

2. ENVIRONMENT

For satellites in a geosynchronous equatorial orbit (GEO), the environment consists of three primary sources of radiation: trapped charged particles, cosmic rays and solar charged particles, see Figure 2.

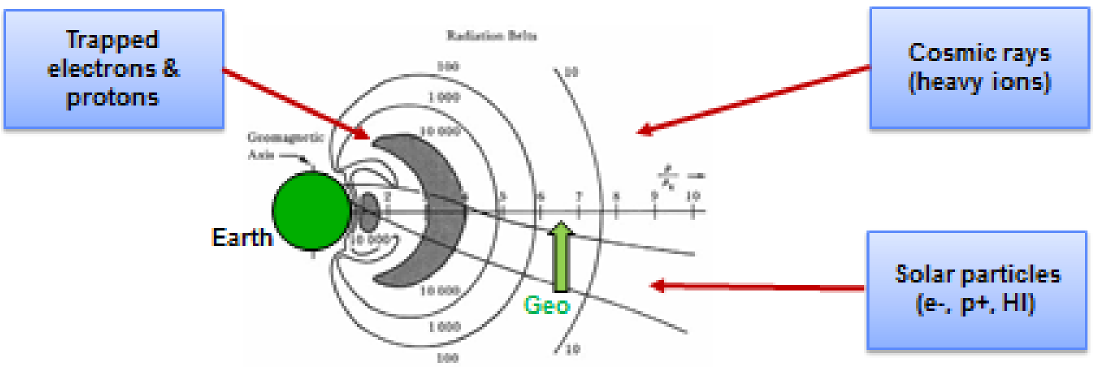

	TID (total ionizing dose)	SEE (single-event effects)	DD (displacement damage)
Cause	Trapped gate & surface state charge	Deposited charge in bulk, space charge regions	Damaged crystal lattice
Effects	Current leakage	Transient current pulse, upset, latchup	Excess charge generation
Testing source	e-, p+, gamma, x-ray	heavy ions, laser pulse	protons, neutrons
Dose unit	rads (100 ergs/gm)	LET (linear energy transfer) in MeV-cm^2-g^{-1}	NIEL (non-ionizing energy loss) in keV-cm^2-g^{-1}

Figure 2. Space radiation environment and effects.

2.1 GEO RADIATION SPECTRAL FLUX

Densities of the various radiation species at all points around Earth have been studied extensively. A static snapshot of the flux for a given point in orbit can be readily calculated based on the models generated from these studies. However, due to the dynamics of the environment—often from minute-to-minute—it is difficult to estimate the radiation accurately.

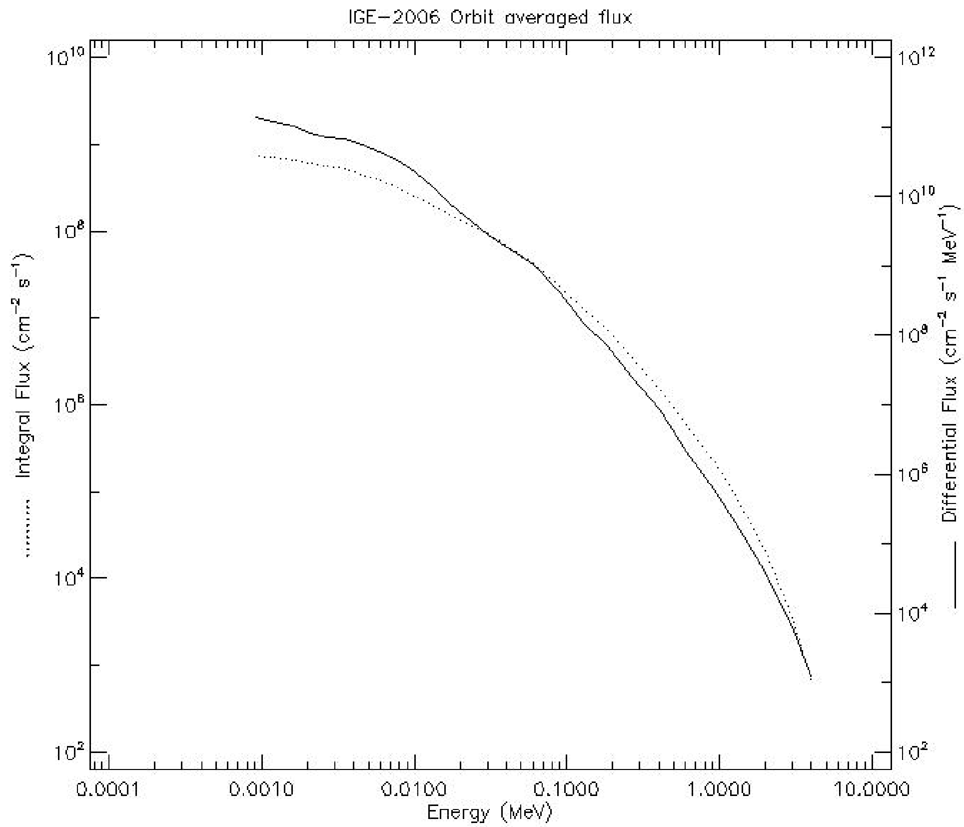

Figure 3. Trapped electron spectral flux from an IGE-2006 model assuming a geosynchronous orbit.

Most of the time at geosynchronous orbit, the only trapped particles encountered are electrons with an energy spectrum shown in Figure 3. This graph shows the energy vs. flux results of IGE-2006 model assuming a geosynchronous orbit as calculated using SPENVIS (Belgian Institute for Space Aeronomy, 2019). This model produces results more applicable to geo orbit than the older AE-8 model. For example, on average, the spacecraft will encounter ~1e5 electrons/cm^2/s with a 1 MeV energy.

Occasionally, due to geomagnetic fluctuations, a burst of protons will be seen, but these are typically not calculated into the overall radiative flux. This is most obvious in the flux maps in Figure 4 and Figure 5, which are based on the AE-8 and AP-8 models; the Earth environment models for electrons and protons respectively. The maps depict a cross-section of the proton and electron concentrations in a geomagnetic coordinate system where the north-south magnetic poles are aligned along the vertical axis. The axes are in units of earth radii. Geo orbit is at ~6.6 Earth radii (along the x-axis). The two major concentrations at R=1.5 and 4.5 radii are the primary Van Allen belts. These graphics were also generated using the SPENVIS website (Belgian Institute for Space Aeronomy, 2019).

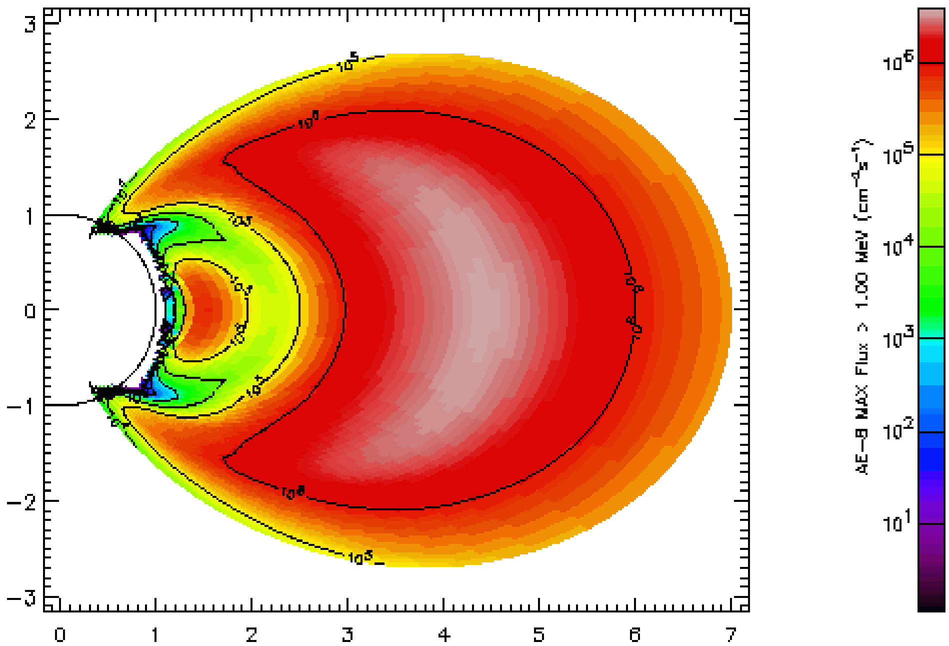

Figure 4. AE-8 cross-section flux map of trapped electron concentrations in a geomagnetic coordinate system.

From the electron map in Figure 4, the flux for electrons > 1.0 MeV is a few times 1E5 /cm^2/sec at geo, which also corresponds with the integral flux in Figure 3. The proton map in Figure 5 shows no protons > 10.0MeV at geo.

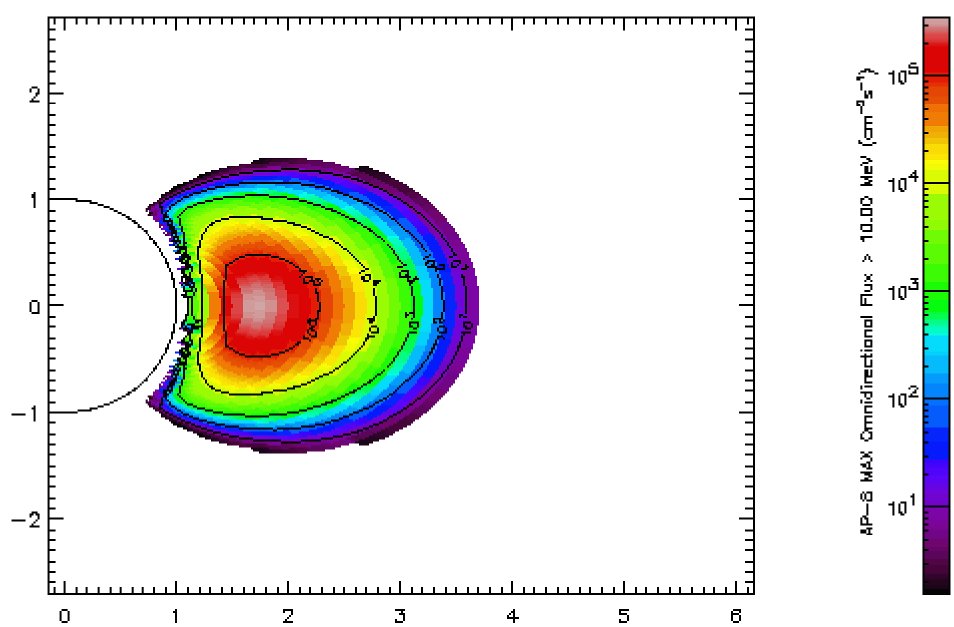

Figure 5. AP-8 cross-section flux map of trapped proton concentrations in a geomagnetic coordinate system.

The highest energy particles encountered at geo are the galactic cosmic rays (GCR). These are ions of elements across the periodic table from hydrogen to uranium. They typically have energies E >> 1 GeV. As can be seen in Figure 6, there is measureable flux for protons to 100 GeV. Some heavier ions can have even higher energies than this. This curve, generated in SPENVIS (Belgian Institute for Space Aeronomy, 2019), uses the CREME96 model. It shows the flux distribution for various proton energies. The x-axis units are MeV/n, which is energy per nucleon. This normalizes the energy for any given atomic species. Iron would have a similar curve but much lower flux.

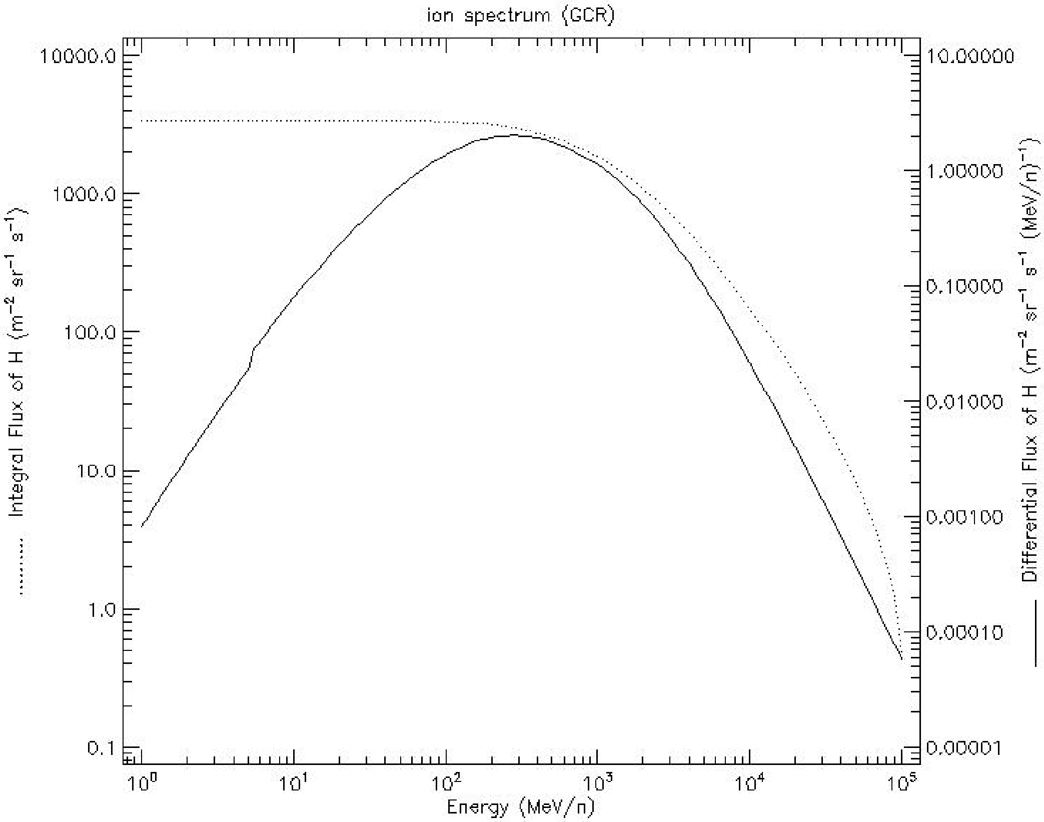

Figure 6. Cosmic ray spectral energy flux.

2.2 TOTAL IONIZING DOSE (TID)-DEPTH CURVES

The previous section presented a discussion of the sources of radiation for the geo environment. The second piece of the measurement is the intervening materials and the device. TID in geosynchronous orbit is delivered by a combination of high-energy electrons, the associated bremsstrahlung radiation and solar protons. Bremsstrahlung are x-rays generated during the interaction of energetic electrons and dense materials such as aluminum. This is illustrated in a dose-depth curve generated on SPENVIS (Belgian Institute for Space Aeronomy, 2019) which assumes a 1-year mission at geo. The dose can be quite variable depending on the date of the mission in relation to the solar cycle. The curve below (Figure 7) is for a quieter portion of the cycle. An order of magnitude increase is possible during solar maximum.

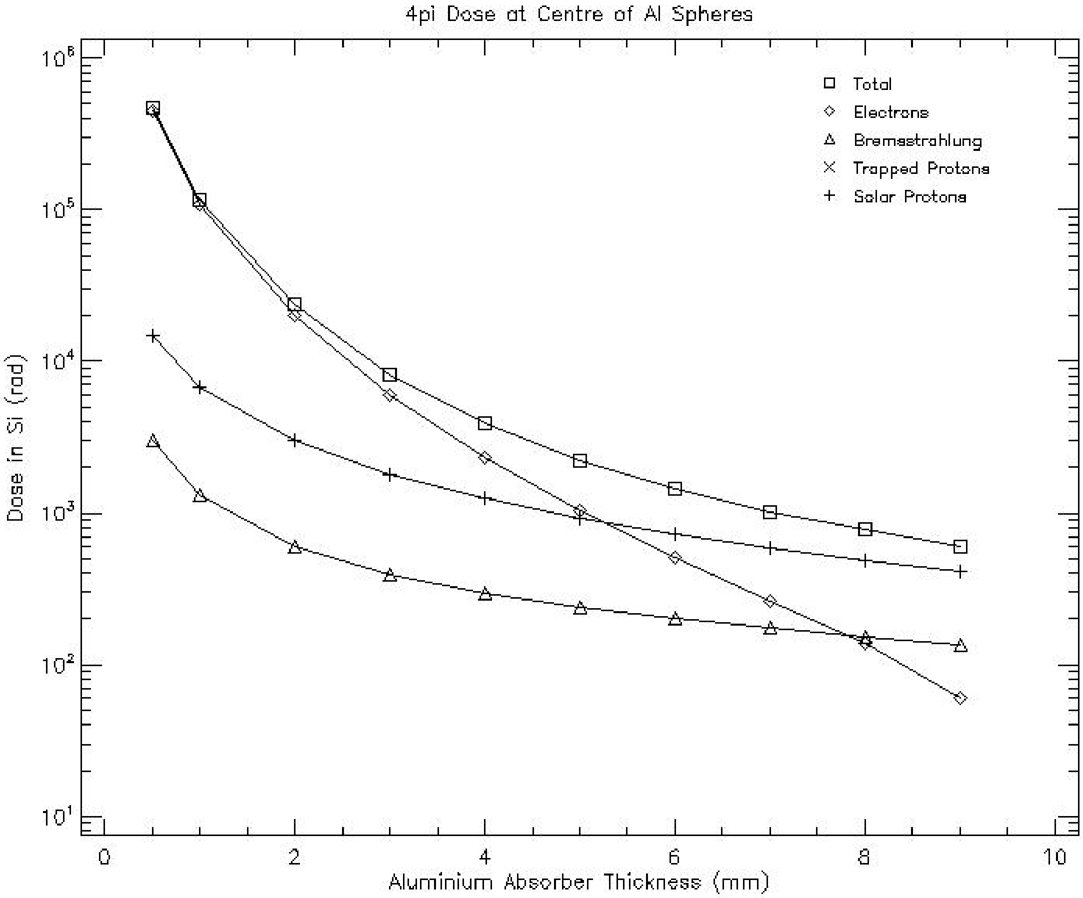

Figure 7. TID radiation components, depth-dose for 1-year mission.

Extending these results to a 5-year mission, which was the sponsor requirement (see Table 7), and over a wider shielding range gives the dose-depth curve of Figure 8.

When working with shielding effects, it is common to use metals with higher densities than aluminum. In this case, the effective aluminum shielding thickness is calculated by multiplying the metal thickness times its density ratio compared to aluminum. Thus, tantalum is ~6x the density of Al, so 1mm Ta = 6mm Al in terms of shielding.

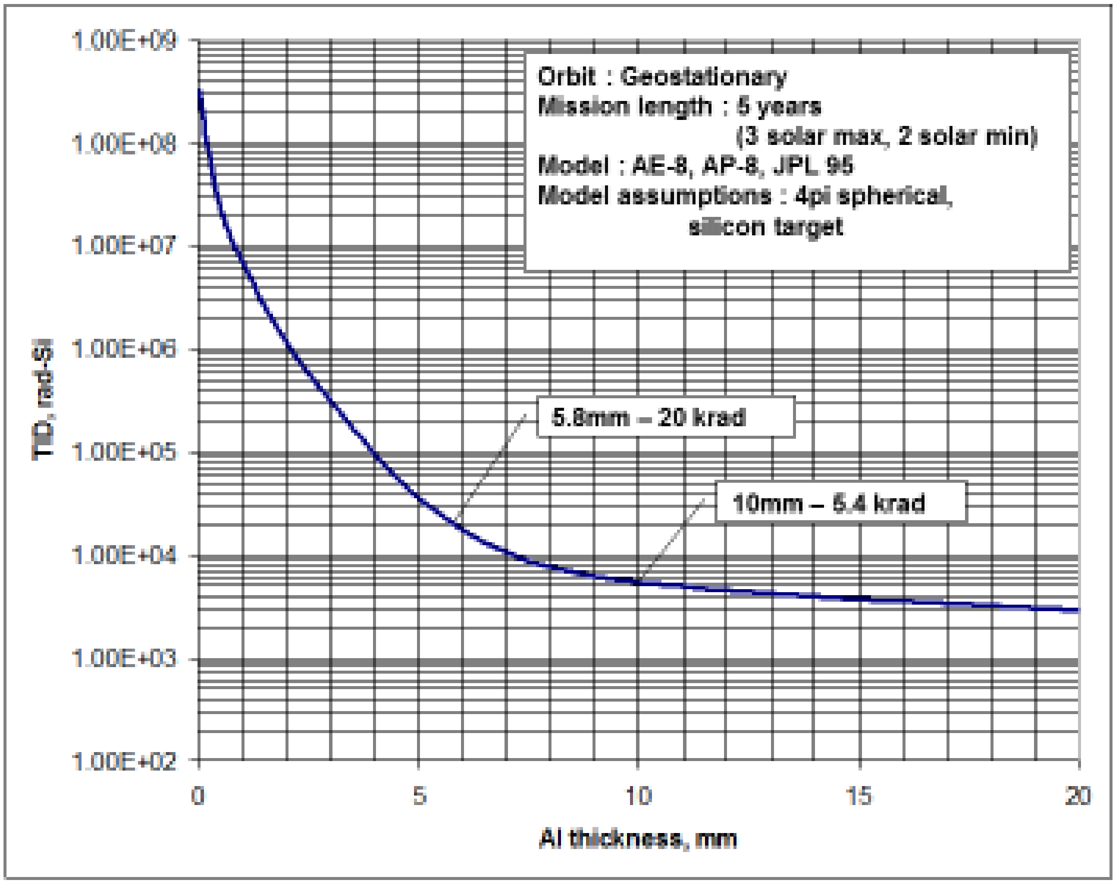

Figure 8. Geo TID dose-depth curve: the relationship between shielding thickness and total ionizing dose for aluminum shielding and silicon target for a 5-year mission.

2.3 SINGLE-EVENT EFFECTS (SEE)

"Single-event effects" is a blanket title for numerous different effects generated in electronic components by high energy particles depositing a large packet of charge in a single location. The most important effects for these tests are single-event latch-up (SEL) and single-event functional interrupt (SEFI). SEL can result in either a damaging condition or one that can be recovered from, but only by shutting off the power to the chip. The second type of event, SEFI, will not damage the chip directly, but may cause either a partial or complete interruption of operation, which may or may not be recoverable.

These types of events are caused primarily by heavy ion radiation with extremely large energies. Occasionally, they can be caused by high energy protons produced by the sun. The mechanism of upset varies depending on the where the energy of the particle is deposited. Wherever energy is deposited, a cloud of charge is generated which results in a change in electrical behavior. In Figure 9, the curve depicts the linear energy transfer (LET) vs. flux out at geo. LET is given here in MeV-cm^2/g, which is a unit normalized for density of material. Once the material's density is known (in most cases silicon), the energy per unit distance can be calculated. The graph in Figure 9 was generated on SPENVIS (Belgian Institute for Space Aeronomy, 2019). This LET range was used to guide the testing conditions chosen (see Test Methodology).

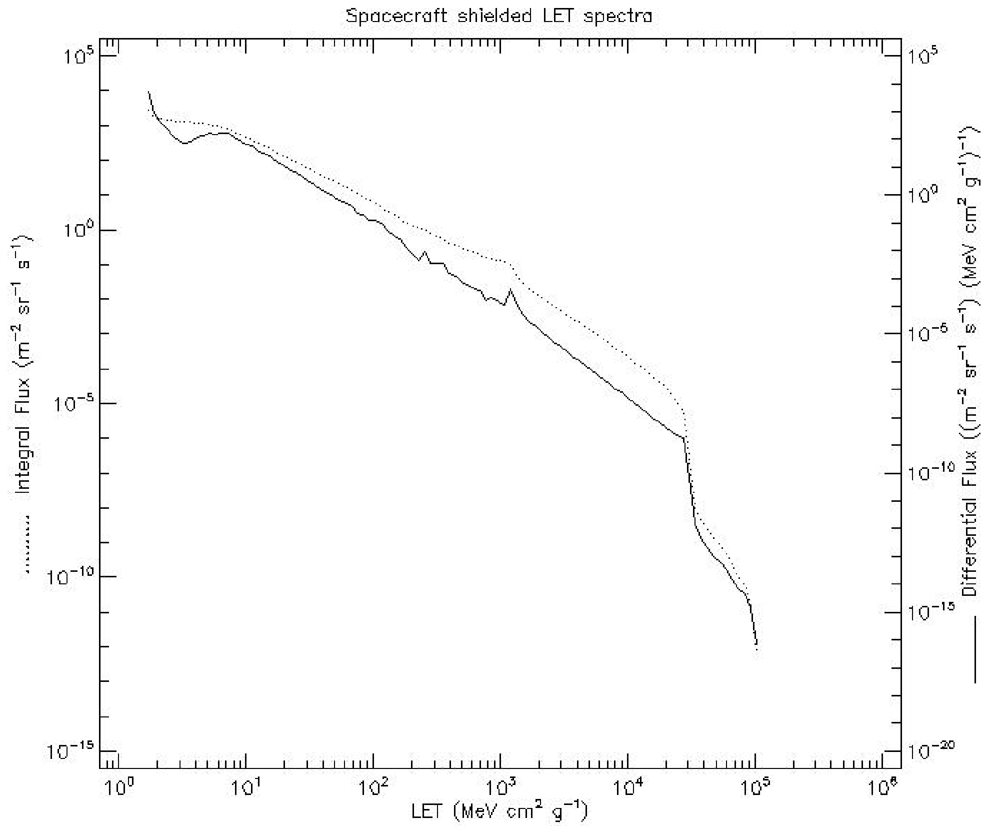

Figure 9. LET spectral flux.

2.4 DISPLACEMENT DAMAGE (DD)

Displacement damage is caused by high energy particles, which strike a semiconductor crystal lattice and dislocate some of the atoms. Dislocations or displacements have a number of effects such as increased dark current and poor charge movement. These effects are most noticeable in optoelectronic semiconductor devices, such as charge-coupled devices (CCDs) and optoisolators. There are also some published reports (Gilard, 2018) (Barde, 2000) of damage to junction detectors which is of concern for this program. This is not an ionization effect. A proton must knock out an atom of the crystal structure. To measure and predict the probability of this requires knowledge of the nuclear cross-section of the material relative to the energy of the proton. In Figure 10, the vertical axis is a measurement of lattice damage relative to that caused by a 95 MeV proton. Note that lower energy protons produce more damage than higher energy ones.

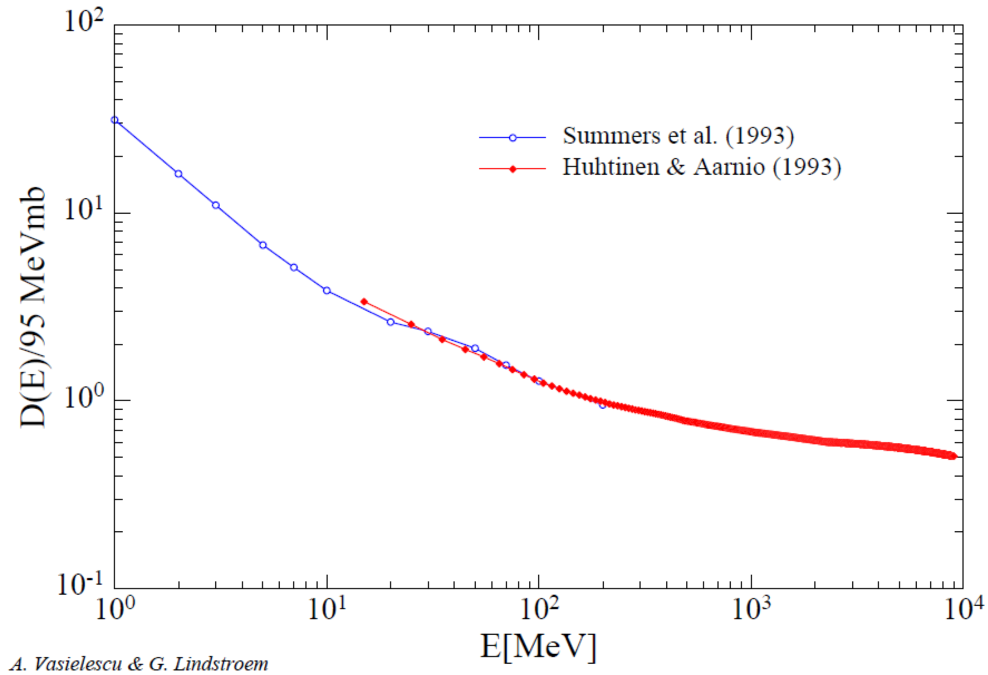

Figure 10. Proton displacement damage in Si. (Vasilescu & Lindstroem, 2000)

One obvious measureable effect of DD is an increase in dark current. In fact, sensitivity to DD for InGaAs detectors has been measured to be three times that of silicon (Gilard, 2018). Thus, our expectation for results from proton irradiation were concerning. A factor which helps in this outcome is that lower energy protons are rare at geo, and shielding helps to a certain extent. How this affects testing will be explained in Section 4.3.

The primary source of displacement damage (DD) are high energy protons (above 10MeV). In particular, for a geo orbit, solar protons and occasionally cosmic rays are these sources, as trapped protons are practically non-existent. The solar proton flux vs. energy data in Figure 11 was generated in SPENVIS (Belgian Institute for Space Aeronomy, 2019) using the CRÈME-96 model. The blue curve represents the modeled proton flux of the worst week on record. The red curve indicates typical proton flux levels. The green vertical line indicates the minimum proton energies, which can penetrate through a common shielding of 2mm aluminum. Assuming a 4π steradians uniform irradiation, for the Digital Tracker Array DFPA's specific area, the fluence at the energy levels available for testing at MGH (70MeV and 160MeV) can be correlated to expected damage in differing time spans. For example, on the worst recorded fluence curve, 70 MeV would correspond to 1 weeks' worth of damage on the DTA DFPA. The 160MeV energy tests had the fluence adjusted to also correspond to a typical 5-year exposure with margin.

Note in Figure 11 that over a mission length of 5-years, the DTA DFPA can expect to see a dose of 2.5e7 (red curve). However, if a repeat of the worst week of solar radiation in measured history occurs (blue curve), an equivalent dose could be deposited in only 1 week. However, this is extremely unlikely.

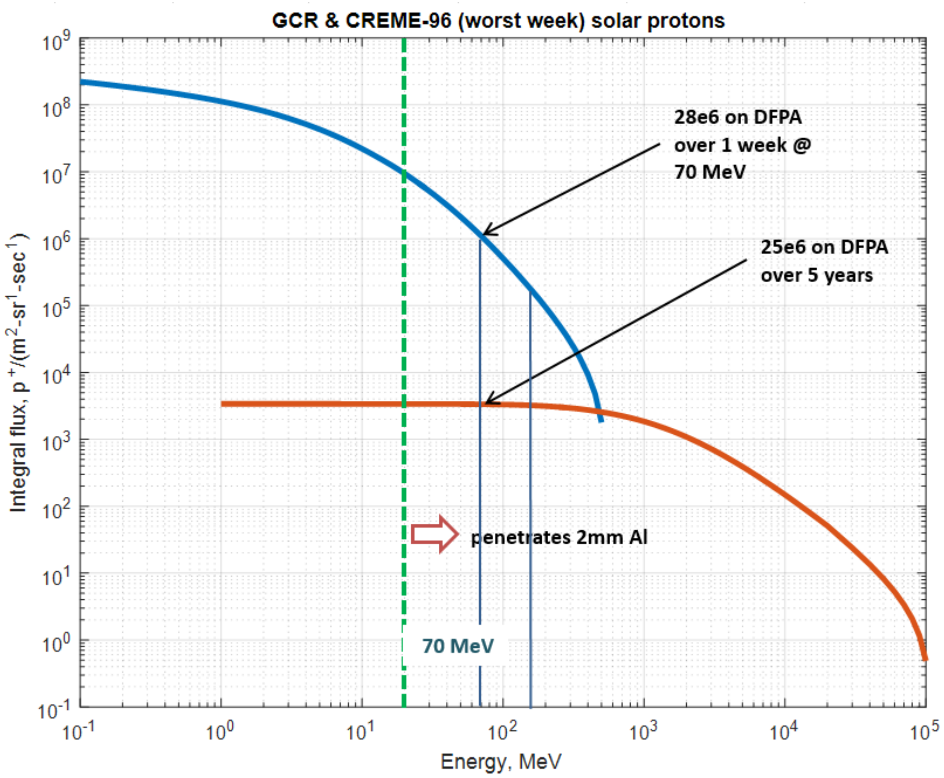

Figure 11. Solar proton energy spectrum.

This page intentionally left blank.

3. COMPONENTS

3.1 TRANSISTOR TEST STRUCTURES

CMOS 10LPe is a CMOS 65 nm generation foundry technology developed for static random access memory (SRAM), logic, and mixed-voltage input/output (I/O) applications. The process offers the following characteristics:

CMOS Process

- VDD of 1.2 V (thin-oxide), VDD = 2.5 V (DG thick oxide)
- Twin- or triple-well (NFET in isolated p-well)
- CMOS technology on p-type substrate
- Shallow trench isolation
- Stress-engineered and optimized devices
- Gate oxide options (2.6 / 2.8 nm [thin, n/p] and 5.7 / 6.0 nm [thick, n/p])
- Minimum drawn gate length of 0.060 μm

Device Options

- Thin-oxide surface channel NFETs and PFETs with a minimum polysilicon gate length1, Lp ≥ 0.057 ± 0.010 μm (see Table 1)
- Thick-oxide devices for 1.8 V, 2.5 V, and 3.3 V operation in I/O applications
- etc.

Voltage and temperature ranges

- Nominal power supply voltage of 1.2 V and 2.5 V (DG) and maximum power supply voltage of 1.32 V and 2.75 V (DG) for thin- and thick-oxide (DG) devices, respectively.
- Operating junction temperature range of -40°C to 125°C
- etc.

Table 1. Transistors Used in DFPA

Type	Func	Width (nm)	length (nm)	W/L	area, 0.001*μm^2
PFET	Std (rvt)	6000	400	15	2400
PFET	Std	120	100	1.2	12
PFET	Std	150	60	2.5	9
PFET	Std	240	60	4.0	14
NFET	Std	6000	400	15.0	2400

NFET	Std	150	60	2.5	9
NFET	Std	240	60	4.0	14
PFET	hvt	500	150	3.3	75
NFET	hvt	500	150	3.3	75
PFET	lvt	50000	120	416.7	6000
PFET	lvt	180	60	3.0	11
NFET	lvt	50000	120	416.7	6000
NFET	lvt	180	60	3.0	11
PFET	dg	40000	280	142.9	11200
NFET	dg	20000	280	71.4	5600

Acronyms used in above table include regular voltage threshold (RVT); low voltage threshold (LVT); high voltage threshold (HVT); double gate (DG).

Test Transistors and Test Structures

We have aggregated an array of transistors and test structures to aid us with our Digital Pixel designs. One of the challenges of operation at 77K is the shift in transistor performance as temperature decreases and the difficulties in developing an accurate cryo model for simulation. We can alleviate some of these difficulties by measuring single transistor performance in the laboratory. We try to cover all possible transistors sizes. These same transistor arrays are used for before/after radiation testing. An aggregated test die, whose layout is shown in Figure 12, consisting of transistors and other structures, was used for before/after exposure measurements. The transistors included in the Test Transistor block are listed in Table 2. These test transistors cover the size and type used in DFPA structures as listed in Table 1.

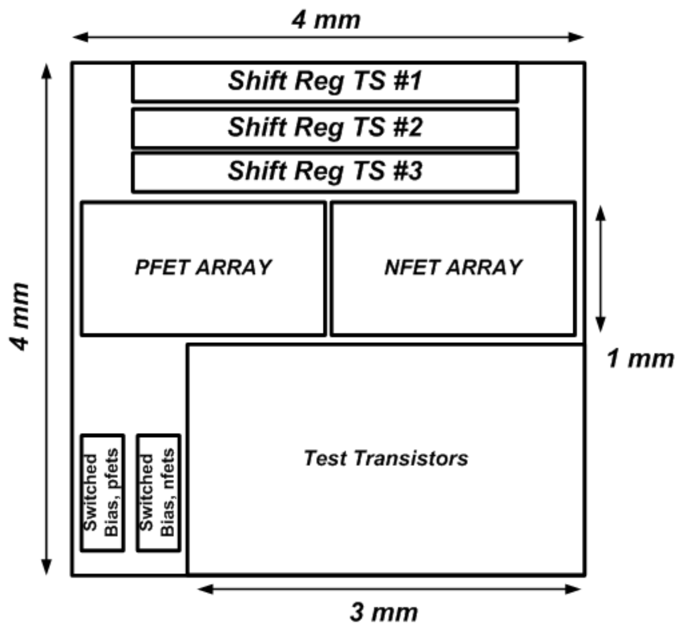

Figure 12. Test chip function blocks.

Table 2. Test Tile Transistor Specifications

	1	2	3	4	5	6	7	8	9	10	11	12	13	14	
	N-fet	P-fet	N-fet	P-fet	N-fet	P-fet	N-fet	P-fet	N-fet	P-fet	N-fet	P-fet	N-fet	P-fet	
G	120n	120n	120n	120n	120n	120n	140n	140n	140n	140n	140n	140n	140n	140n	Width
	60n	60n	2u	2u	2u	2u	60n	60n	60n	60n	2u	2u	2u	2u	Length
	lvt	lvt			lvt	lvt			lvt	lvt			lvt	lvt	Type
F	8u	8u	400n	400n	1.44u	1.44u	400n	400n	120n	120n	2u	2u	120n	120n	
	8u	8u	280n	280n	280n	280n	960n	960n	60n	60n	250n	250n	60n	60n	
	lvt	lvt	dgn	dgp	dgn	dgp	dgn	dgp	hvt	hvt	hvt	hvt			
E	2u	2u	2u	2u	2u	2u	2u	2u	2u	2u	2u	2u	8u	8u	
	500n	500n	500n	500n	1u	1u	1u	1u	2u	2u	2u	2u	8u	8u	
			lvt	lvt			lvt	lvt			lvt	lvt			
D	2u	2u	2u	2u	2u	2u	2u	2u	2u	2u	2u	2u	2u	2u	
	80n	80n	140n	140n	140n	140n	160n	160n	160n	160n	250n	250n	250n	250n	
	lvt	lvt			lvt	lvt			lvt	lvt			lvt	lvt	
C	500n	500n	500n	500n	1u	1u	1u	1u	2u	2u	2u	2u	2u	2u	
	2u	2u	2u	2u	2u	2u	2u	2u	60n	60n	60n	60n	80n	80n	
			lvt	lvt			lvt	lvt			lvt	lvt			
B	140n	140n	180n	180n	180n	180n	240n	240n	240n	240n	300n	300n	300n	300n	
	2u	2u	2u	2u	2u	2u	140n	140n	140n	140n	2u	2u	2u	2u	
	lvt	lvt			lvt	lvt			lvt	lvt			lvt	lvt	
A	120n	120n	120n	120n	120n	120n	120n	120n	140n	140n	140n	140n	140n	140n	
	60n	60n	60n	60n	2u	2u	2u	2u	60n	60n	60n	60n	2u	2u	
			lvt	lvt			lvt	lvt			lvt	lvt			

3.2 READOUT INTEGRATED CIRCUIT (ROIC)

3.2.1 General: Digital Pixel Focal Plane Array (DFPA) and Digital Readout Integrated Circuit (DROIC) at MIT Lincoln Laboratory

ROICs, or, readout integrated circuits, are used in the imaging field to provide an electrical interface to an array of detectors and multiplex the signal from each detector into data stream or video stream which can be processed and displayed. The DROIC designed at Lincoln Laboratory utilizes an analog to digital convertor (ADC) in every pixel as part of the detector/ROIC interface circuit. The outputs of these convertors are digitally multiplexed onto a high-speed digital output. The pixel ADC of the DFPA are single-bit oversampling converters. These convertors utilize a scene-modulated pulse stream, fed into a digital counter, generating a distinct digital word for every flux level. These counters are composed of memory nodes, also referred to as master slave flip-flops or as registers. The term register comes about in that, in addition to maintaining memory, they register the digital word to a falling clock edge.

The multiplexers, which convert the many columns to one output, are also composed of these flip-flops, or, registers. Additionally, the configuring bits mentioned earlier are also memory nodes.

Pixel-level digitization improves signal to noise and gives the data the ability to shift in any orthogonal direction without degradation to the signal to noise. This is especially useful for data manipulation applications, such as time-delayed integration (TDI), digital correlated double-sampling (CDS), or other kernel filtering functions.

From the perspective of susceptibility to event upset, the MIT LL ROICs can be considered as an array of many storage registers. In each pixel, there are dual-purpose registers which count and/or shift data and SRAM for pixel-level settings. There are non-uniformity correction (NUC) registers to initialize the counters, and configuration registers for setting "once per operation" bits, e.g., number of outputs, clock input, etc. These registers are listed in Table 3Table 3, and their location is shown in Figure 13. An upset can change the state of the storage node, and the impact these upsets have on the operation of the ROIC depends on the function of that particular register. The SRAM, NUC, configuration, and header registers are set once at the startup of the focal plane and if these registers become corrupted during operation, the focal plane will require another startup initialization for proper operation. The counter/shift registers are reset at the frame rate and so any potential corruption would be corrected at the next frame.

Table 3. Summary of Configuration Bits and their Functions

Configuration Bits	Function
Pixel-level SRAM	Pixel-level settings, redundant input, gain, disable
NUC Input Registers	Pixel-level counter initiation, SRAM write
Configuration and Header Bits	Startup settings. Number of outputs

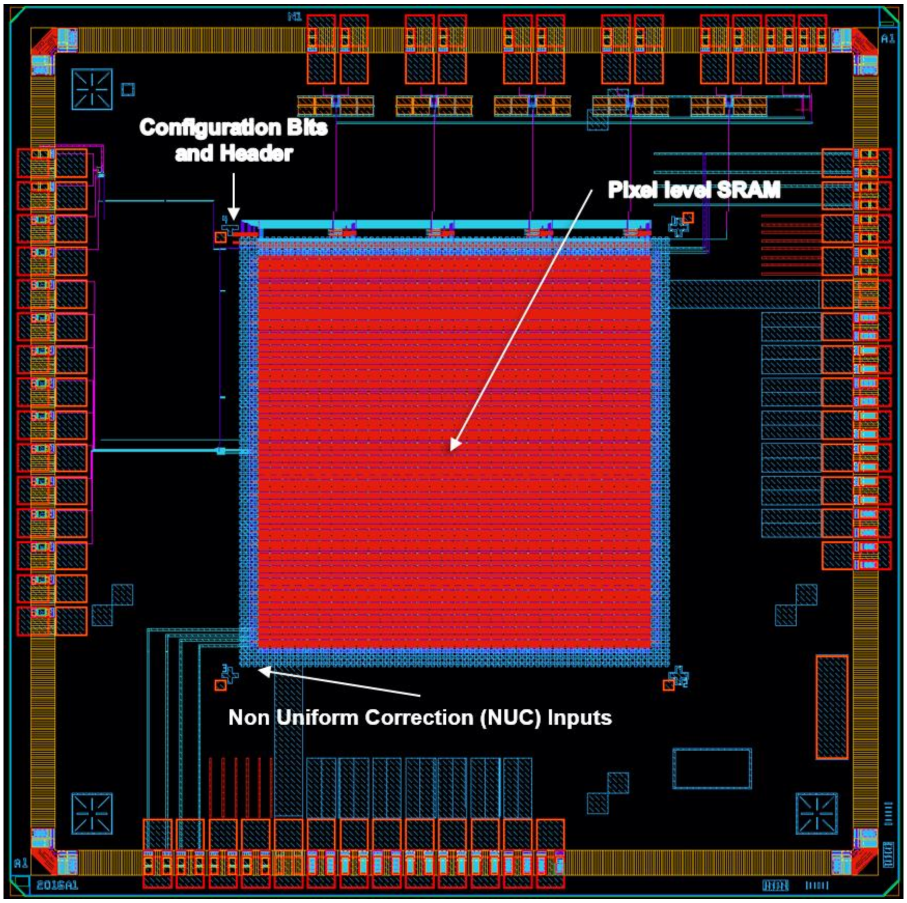

Figure 13. Location of storage registers of the DTA ROIC.

3.2.2 Radiation Susceptibility in DROICs: Process, Electrical Design, Physical Design

The current DROICs are designed in the Global Foundries 65 nm process. The small feature size of this process is naturally somewhat resistant to radiation damage due to the inherent small transistor cross-sections and corresponding lower probability of collisions. However, particles colliding with silicon atoms in the substrate can generate a large slug of minority carriers, which can switch on the parasitic bipolar silicon controlled rectifier (SCR) type structures. Since this turn on requires some finite amount of resistance in the substrate, we can reduce latch-up susceptibility by adding large amounts of substrate connections, thereby reducing this resistance and allowing any free minority carriers to be quickly swept up. There is an additional benefit with strong substrate connections in that it boosts the connection to the well/substrate junction, which is arguably the best bypass capacitance available in this process. Figure 14 shows the long n-well and substrate contact where every transistor is within 1µm to a substrate contact.

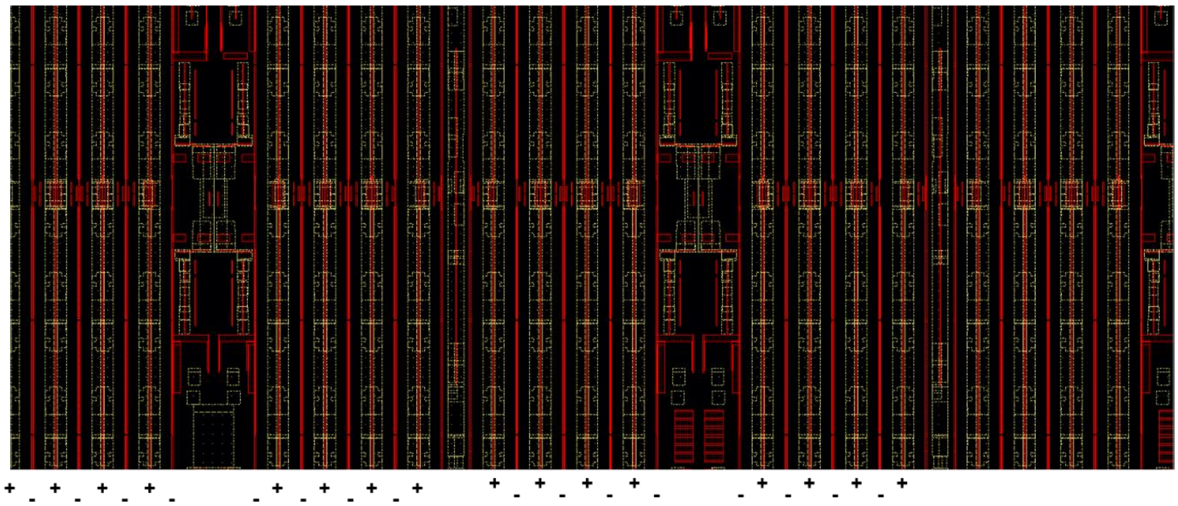

Figure 14. Layout example of substrate contacts showing the proximity of transistors to substrate contacts: the yellow-delineated areas are n-wells, and the red lines indicate long rows of contacts to substrate and n-wells. The spacing between the red vertical lines is 5 µm.

3.2.3 DROIC Hardening by Design

There were two considerations in designing for a radiation-challenged environment. The first is handling the flipping of bits in the storage nodes around the ROIC. The second is keeping the parasitic bipolar devices from turning on and causing a high current latch-up. We addressed the bit flip issue by replacing any and all registers that are not reset every frame by hard-wired choice. This hard-wired replacement removes all programmability of the DFPA and now the ROIC design will be targeted toward the specific operation of this program. This involves setting the value of the NUC, number of outputs, header value and so on, by design.

The second consideration for a radiation environment is latch-up, and here the substrate connections were reviewed and augmented. The number of substrate contacts was maximized for the given space, as is typical for the ROIC design process.

There were three design cycles on this program: Spin 0, Spin 1, and Spin 2. The main goals for each spin are outlined in Table 4. There were several design variants within Spin 1 and Spin2 but the variations within each spin were expected to have no impact on radiation response.

Table 4. Summary of ROIC Design Cycles

Design Cycle	Features	Goals of Design Changes	Date	Sizes	Run name
Spin 0	Gate-modulated input, current mirror gain	High Gain, Low Capacitance Current Gain	2015	64 x 64	DFPA66_2015B_10LPe
Spin 1	Buffered direct injection/ buffered gate modulated	Detector Bias Control, Radiation Hardening	Nov 2016	64 x 64, 128 x 128	DFPA66_2016ABx_10LPe
Spin 2	**Buffered direct injection/ fully independent counters**	**Thermal Balancing, Independent Counter Control**	**July 2017**	**64 x 64**	**DFPA66_2017Cx_10LPe**

3.3 DETECTORS

The photodiodes utilized in this effort are InGaAs/InP arrays fabricated by FLIR. Both 64 x 64 and 128 x128 array formats were fabricated with a 30 µm pitch. The manufacturer uses the standard p-on-n design, where n-type InP and InGaAs epitaxial layers are grown on an InP substrate and p-regions are formed by diffusion of Zn through the top n- InP window layer. Although the manufacturer does not share the exact details of the epitaxial layers (doping, thickness, etc.), a cross-sectional drawing of this nominal design for a single pixel is shown in the left side of Figure 15. Fabricated in this manner, the pixels are contiguous with no dead region (100% fill factor). Common n-contacts for each array are located at the periphery, as shown on the right hand side of the figure.

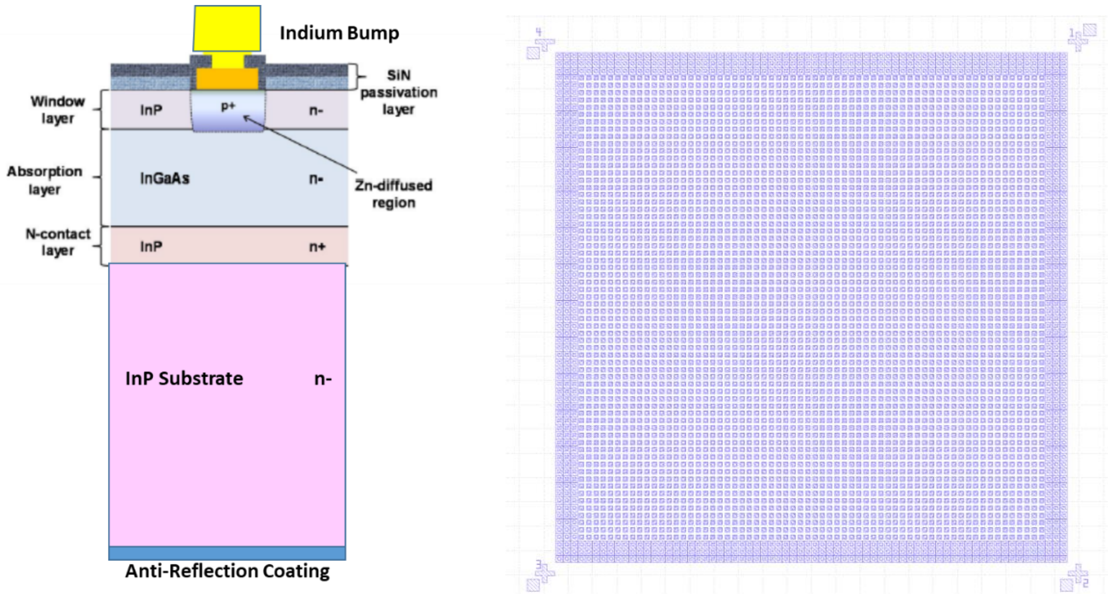

Figure 15. (Left) Typical cross-section of InGaAs photodiode (based on SPIE Proceedings 945105-1, A. Rouvie et al, 2015); (right) 64 x 64 array layout showing pixel contacts and common contacts around periphery.

The two primary metrics for InGaAs photodiodes are quantum efficiency (QE) and dark current (Id). Secondary metrics that may become important in some cases include diode capacitance, electrical bandwidth, and crosstalk between pixels. These secondary metrics are not addressed further here. QE will be addressed first and then dark current.

QE is the product of photon absorption efficiency and photo-carrier collection efficiency. For the DTA InGaAs arrays, the manufacturer designed the structure to enable high (>85%) QE at 1564 nm. This was accomplished through selection of appropriate InGaAs thickness, use of low-loss InP substrates and tailoring of the AR-coating applied to the back surface of the substrate to reduce loss of photons prior to entry into the primary photon absorbing InGaAs portion of the device. The cross-sectional drawing of a typical InGaAs photodiode shows each of these components. The results of this optimization allowed the demonstration of 90% QE in the delivered devices. To realize this level of QE, the photocarrier collection efficiency must also be at least 90% (under the operating bias conditions used for the measurement).

In considering the potential impact of radiation on QE it is useful to evaluate each of the two QE factors separately, absorption efficiency and collection efficiency. To first order, radiation exposure at low to moderate doses would not be expected to change the absorption efficiency. At very high radiation dose levels where the primary InGaAs atomic lattice could be disturbed significantly, the absorption characteristics of the InGaAs would be expected to change. Similarly, at very high doses the effective carrier concentration in the InP substrate and integrity of the anti-reflection coating could also change, adding to free-carrier absorption and reflection losses. Under the radiation exposure levels explored in this program, none of those secondary effects are expected.

Photocarrier collection efficiency could be impacted by radiation exposure through multiple mechanisms. Two of these possibilities are a reduction in photocarrier collection due to a reduction in carrier lifetime and a reduction in carrier collection due to a modification of the electric fields in the photodiode.

Dark current is the result of various carrier generation and collection mechanisms in the photodiode, including bulk generation-recombination (G-R) in the InGaAs and InP semiconductor layers within and near the photodiode, surface recombination, field-enhanced tunneling and surface charge migration among other contributions. Measurements on the DTA photodiodes prior to radiation exposure show dark current levels at room temperature consistent with high-quality (long lifetime) InGaAs layers and well-passivated surfaces. Since operation of the photodiodes is at low bias voltage, field-enhanced tunneling in these devices is low.

The strongest impact of radiation exposure on photodiodes is typically found to be an increase in dark current. The primary mechanism responsible for the increase in dark current is often found to be a drop in carrier lifetime (due to damage to the crystal lattice) leading to an increase in G-R current, but could also be a change in surface or edge leakage (due to ionizing radiation induced change in surface and field conditions). Depending on the details of the device design and operation, either of these contributions could dominate the radiation-induced dark currents.

3.4 VOLTAGE REGULATORS

The voltage regulators used in the DTA test board were Linear Technology Lt3021-ADJ VLDO regulators in an 8-lead plastic SO package. The voltage regulators were exposed to two types of radiation testing. Heavy ion testing at Texas A&M University (TAMU) and gamma ray testing at University of Massachusetts Lowell (UML). In both cases, a source measurement unit (SMU) recorded voltage regulation and current measurements before and after irradiation, while the TAMU testing was also measured during irradiation. The regulators were also gamma irradiated measuring output voltage before, during, and after irradiation. Figure 16 outlines some of the characteristics provided by the manufacturer.

FEATURES

- **V_{IN} Range: 0.9V to 10V**
- **Dropout Voltage: 160mV Typical**
- **Output Current: 500mA**
- **Adjustable Output ($V_{REF} = V_{OUT(MIN)} = 200mV$)**
- **Fixed Output Voltages: 1.2V, 1.5V, 1.8V**
- Stable with Low ESR, Ceramic Output Capacitors (3.3µF Minimum)
- 0.2% Load Regulation from 0mA to 500mA
- Quiescent Current: 120µA (Typ)
- 3µA Typical Quiescent Current in Shutdown
- Current Limit Protection
- Reverse-Battery Protection
- No Reverse Current
- Thermal Limiting with Hysteresis
- 16-Pin DFN (5mm × 5mm) and 8-Lead SO Packages

DESCRIPTION

The LT®3021 is a very low dropout voltage (VLDO™) linear regulator that operates from input supplies down to 0.9V. This device supplies 500mA of output current with a typical dropout voltage of 160mV. The LT3021 is ideal for low input voltage to low output voltage applications, providing comparable electrical efficiency to that of a switching regulator.

The LT3021 regulator optimizes stability and transient response with low ESR, ceramic output capacitors as small as 3.3µF. Other LT3021 features include 0.05% typical line regulation and 0.2% typical load regulation. In shutdown, quiescent current typically drops to 3µA.

Internal protection circuitry includes reverse-battery protection, current limiting, thermal limiting with hysteresis, and reverse-current protection. The LT3021 is available as an adjustable output device with an output range down to the 200mV reference. Three fixed output voltages, 1.2V, 1.5V and 1.8V, are also available.

The LT3021 regulator is available in the low profile (0.75mm) 16-pin (5mm × 5mm) DFN package with exposed pad and the 8-lead SO package.

Figure 16. Linear Technology LT3021-ADJ VLDO regulator in an 8-lead plastic SO package.

4. TEST METHODOLOGY

4.1 TID

To determine the susceptibility of an electronic part to ionizing radiation, a test must deposit a specified range of energies in the different layers of the component. Rather than do this with three separate tests (electrons, protons and x-rays), a single test using gamma radiation can be performed.

A common source of gamma radiation for TID tests is a cobalt-60 (Co-60) source which produces gamma rays of 1.25 MeV on average. Most of these photons pass through the silicon of an IC without being absorbed. However, those that are absorbed provide an easily controllable dose rate based on distance from the source, strength of source, and structure size. The testing levels were determined by correlating to a hypothetical 5 year mission.

For gamma testing, no special preparation of the components is required. The parts are positioned so the normal of the silicon surface is pointing at the source. The distance from the source is a calculated value, usually based on calibrated tables for the particular facility. Typically, more than one component can be tested at a time since Co-60 acts as a point source. One important test requirement is that the devices must be powered during irradiation. This allows migration of hole-electron pairs generated in gate structures to occur.

Gamma ray testing of the voltage regulators used a linear power supply and resistive load during irradiation. A source-measurement unit (SMU) recorded voltage regulation and current measurements but only before and after irradiation.

4.2 SEE (SINGLE EVENT EFFECTS)

The primary concern in SEE testing was the possibility of an SEL (single event latch-up) occurring during mission operations. Consequently, all components were to be evaluated for SEL susceptibility. Ideally, an effective cross-sectional area for SEL and other SEE is derived by counting the number of events for a given fluence over the mission's linear energy transfer (LET) range (see Figure 9). In practice, this can be challenging, if not problematic, depending on whether the effect of interest is present or identified. SEL as defined here is reasonably straight forward to identify as the current levels were monitored.

Heavy ions used for these tests have ranges in silicon of between 150–200 µm. This limitation requires that the bare silicon be exposed to the beam. In the case of the ROIC, this is not a problem. A hybridized DFPA will only have the detectors exposed, however. As an aside, the test method using heavy ions does not emulate the space environment in terms of particle type. It only reflects the effective LET of the wide spectrum of extremely high energy particles in the environment. The test conditions were chosen to be cover the span of LET range while the fluence conditions were to maximize measureable events.

In order to increase the number of LET levels tested for a given species energy, an increase in LET can be achieved by increasing the angle of the beam off the ROIC normal. Simply, this has a $1/\cos\Theta$ effect where theta is the angle off-normal. Theta is usually kept to < 60 degrees.

Heavy ion testing of the voltage regulators used a SMU as a source and a load for the regulators. The SMU recorded regulator voltage and current at both input and output before, during and after irradiation. The test for regulation used a 5 mA and 100 mA current load to verify constant voltage of a large range. The regulators were de-lidded before exposure to heavy ions.

4.3 DD (DISPLACEMENT DAMAGE)

Testing for the effects of displacement damage requires the exposure of the device under test (DUT) to high energy protons. The Francis Burr Proton Beam Therapy Center at Massachusetts General Hospital was used for DD testing. The beam's parameters are shown in Table 5. Note that over the energy range of the beam as plotted on the relative damage curve in Figure 11, the DD may increase by a factor of two or three. Therefore, testing at two energy levels is considered sufficient and, depending on time and resources, a single energy level is often used.

Proton energies for these tests were 70 and 160 MeV. Models for the environment (see Figure 11) show for a 5-year mission, the expected dose of high energy protons will be ~2.5e7 protons. Given a single worst-week scenario, this dose could double to 5.0e7 protons. A conservative margin of 3x would therefore give testing dose levels to 1.5e8 protons. As is shown in Table 10, using the area of the FPA, the desired fluence in protons/cm^2 allows the calculation of irradiation times. A program-level decision was made to dose at 3 stages of 1x, 3x and 9x expected values.

Table 5. MGH Proton Beam Parameters

Energy	70 - 230 MeV
Emittance (adjustable)	15 - 30 mm-mrad
ΔE/E (adjustable)	± 1%
Time Structure	Continuous/pulsed
Rf Frequency	106 MHz
Beam Current	<300nA at full energy
Intensity Dynamic Range	1000:1 (15 μsec)
Time to Change Rooms	2 minutes
Time to Change Energy	~ seconds
Access Wait Time	Immediately after beam off

Finally, a number of performance parameters for the DFPA must be selected. For DD, a common parameter is dark current. Therefore, after each exposure, a dark count measure was made. In addition, some degradation of the detector diodes is expected. Along with dark current, a measure of quantum efficiency (QE) was made.

5. TEST CAMPAIGN

5.1 X-RAY SOURCE FOR TRANSISTOR TID

5.1.1 X-ray TID Testing Of Transistor Structures

Tests were performed in late 2015 to determine TID susceptibility of basic transistor structures. This was a gating decision as to whether or not to move on to further testing if the transistors demonstrated sufficient radiation hardness.

The Aracor Semiconductor Irradiation System (Model 4100) provides the capability to irradiate semiconductor devices with low energy x-rays. The dose rates available from the Aracor are listed in Table 6. The probe station uses a 150mm (6 inch) chuck to hold a wafer. The device under test (DUT) is measured using a 4-needle probe card. The probe card must be designed for the specific pad pitch of the DUT. Cables from the probe card are connected to the Agilent 4155 semiconductor analyzer.

Table 6. Aracor Dose Rate

NOMINAL VALUES (from ARACOR Chart)										
Power Supply	Power Supply Voltage (kV)									
Current (mA)	20		30		40		50		60	
	Dose Rate (per min.)		Dose Rate (per min.)		Dose Rate (per min.)		Dose Rate (per min.)		Dose Rate (per min.)	
	kRAD(Si)	kRAD(SiO_2)	kRAD(Si)	kRAD(SiO_2)	kRAD(Si)	kRAD(SiO_2)	kRAD(Si)	kRAD(SiO_2)	kRAD(Si)	kRAD(SiO_2)
0.5	0.40	0.22	0.90	0.50	1.40	0.78	1.90	1.06	2.30	1.28
1	0.80	0.44	1.90	1.06	3.00	1.67	3.90	2.17	4.70	2.61
2	1.80	1.00	3.90	2.17	6.10	3.39	8.10	4.50	9.70	5.39
5	4.50	2.50	10.00	5.56	15.60	8.67	20.40	11.33	24.80	13.78
10	9.00	5.00	20.40	11.33	31.30	17.39	41.20	22.89	49.90	27.72
20	18.70	10.39	41.60	23.11	62.80	34.89	83.70	46.50	100.00	55.56
40	38.40	21.33	85.60	47.56	130.00	72.22	170.00	94.44	205.00	113.89
58	NULL	NULL	118.00	65.56	182.00	101.11	239.00	132.78	290.00	161.11
80	NULL	NULL	170.00	94.44	240.00	133.33	NULL	NULL	NULL	NULL

$RAD(SiO_2) = RAD(Si) / 1.8$

5.2 GAMMA SOURCE IRRADIATION FOR TID

Gamma testing occurred at the University of Massachusetts Lowell Radiation Laboratory (UML). Two rounds of testing were conducted at this facility in August 2016 and in August 2017. The 2016 test evaluated the performance of the Spin 0 chip and the 2017 test investigated the performance of the Spin 1 chip, which was modified for radiation hardness. The 2017 test also included testing of the de-lidded voltage regulators. The radiation environment specifications and a 2x margin guided the targeted doses at the UML tests and are listed in Table 7.

Table 7. Radiation Requirements for Gamma Testing

Year	Dose	2x
1	25 krad	*50 krad*
2	50 krad	*100 krad*
3	75 krad	150 krad
4	100 krad	200 krad
5	125 krad	250 krad

Original Radiation Environment

Year	Dose	2x
1	*100 krad*	*200 krad*
2	*200 krad*	*400 krad*
3	300 krad	600 krad
4	400 krad	800 krad
5	500 krad	1 Mrad

Alternate Radiation Environment

Duplicates in italics

5.3 HEAVY ION IRRADIATION FOR SEE

Testing with heavy ions took place at Texas A&M University (TAMU) at their heavy ion beam accelerator. The first series of measurements for determining susceptibility to SEL (single event latch-up) were performed on April 14, 2016. The list of useful ions, shown in Table 8, were chosen to span the maximum range of LET and minimize the number and size of gaps between energies (see Figure 17). The number of devices to be tested could result in a very large test matrix; therefore, a subset was selected during test to emphasize the SEL priority, i.e., higher energy ions. As time permitted, lower LETs were to be used to explore other SEEs. The subset is outlined in red in the table. To best capture measureable events, the fluence levels were maximized.

Table 8. TAMU Ion Selection Series

Ion list				Effective LET @ angle degrees			Range depth (um) in Si @ angle		
Index	Element	Symbol	LET, normal incidence (MeV-cm^2/mg)	0	30	45	0	30	45
1	Tantalum	Ta	74.8	74.8	86.4	105.8	155	134	110
2	Praseodymium	Pr	56.0	56.0	64.7	79.2	154	133	109
3	Silver	Ag	40.3	40.3	46.5	57.0	156	135	110
4	Krypton	Kr	26.6	26.6	30.7	37.6	170	147	120
5	Copper	Cu	18.7	18.7	21.6	26.4	172	149	122
6	Argon	Ar	8.0	8.0	9.2	11.3	229	198	162
7	Neon	Ne	2.6	2.6	3.0	3.7	316	274	223

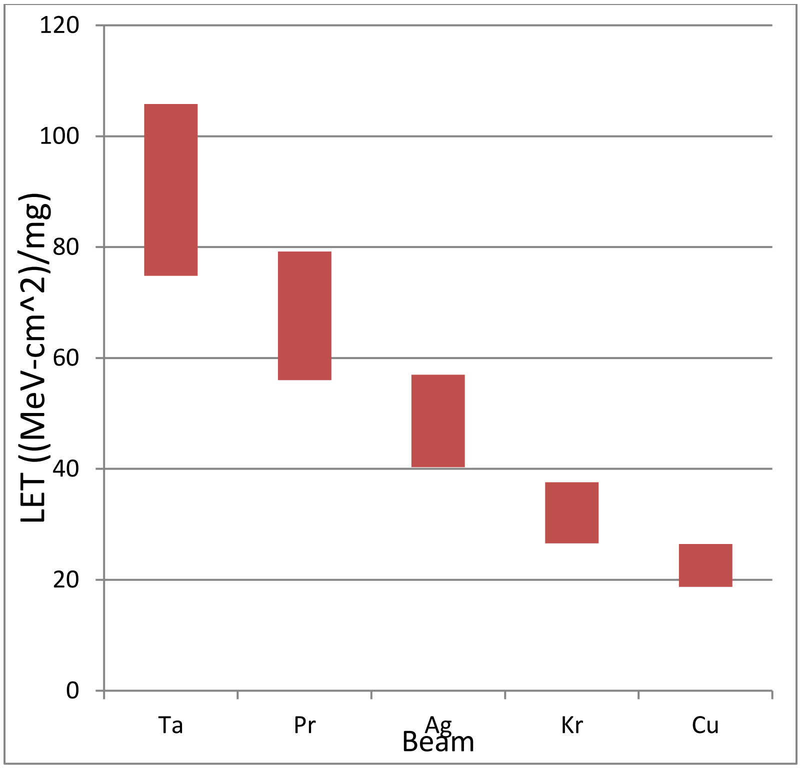

Figure 17. Selected ion LET coverage.

The second round of testing was designed to explore the single-event upsets (SEU) or more accurately single-event functional interrupts (SEFI). This test series took place a year later on May 2017. The first series had determined the ROIC was not susceptible to latch-up. However, there were considerable SEFI events, which needed to be investigated. To establish a cross-section for these events, measurements needed to be made with lower LET ions. A third test series took place in September of 2018. The purpose of this final test was to confirm that layout changes made in the Spin 2 ROIC design did not compromise the radiation hardness of the chip.

5.4 PROTON IRRADIATION FOR SEE & DD

Three rounds of proton testing took place at the Francis H. Burr Proton Therapy Center at Massachusetts General Hospital. The first round of testing in June 2016 evaluated the performance of the Spin 0 ROICs and ROICs bonded with InGaAs detector arrays (hybrids). The second round in June 2017 focused on the Spin 1 ROICs and ROIC/InGaAs hybrids. The third and final round in September 2018 consisted of testing the Spin 2 ROIC and the voltage regulators.

This page intentionally left blank.

6. TESTING RESULTS

6.1 TRANSISTOR X-RAY TEST

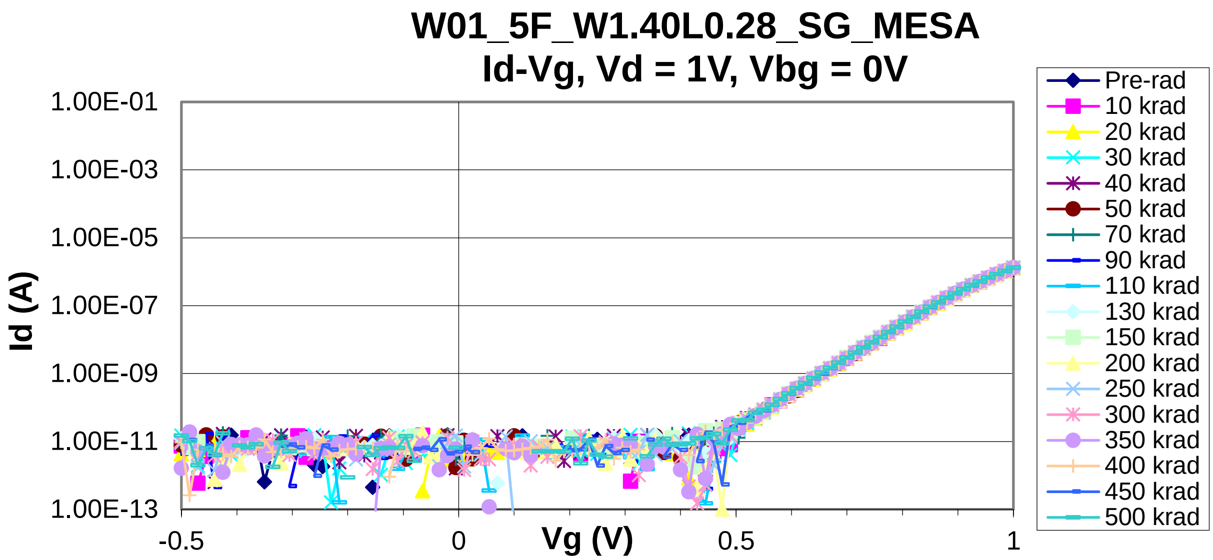

Figure 18. Transistor TID test result.

As shown in Figure 18, all transistor test structures for a double gate transistor 1.44 microns in width and 0.28 microns in length exhibited no measureable changes in I-V curves up to 500 kRad of TID. In fact, these results coincide well with other industry measurements, which show TID hardness well into the Mrad range (Roche, 2009).

6.2 SENSOR & REGULATOR TEST RESULTS

6.2.1 Test Timeline

Testing results will be reviewed chronologically, as they appear in Table 9.

Table 9. Summary of Radiation Test Campaign

Devices	Radiation type	Facility	Date	Effect	Purpose
Spin 0 ROIC	Heavy ion	TAMU	April 2016	SEE	Latch-up, SEFI
Spin 0 Hybrids, ROIC	Proton	MGH	June 2016	DD	Latch-up, dark current
Spin 0 Hybrids, ROIC	Gamma ray	UML	Aug 2016	TID	Dark current, response
Spin 1 ROIC	Heavy ion	TAMU	May 2017	SEE	Latch-up, SEFI

Spin 1 Hybrids, ROIC	Proton	MGH	June 2017	DD	Latch-up, dark current
Spin 1 Hybrids, ROIC, regulators	Gamma ray	UML	Aug 2017	TID	Dark current, response
Spin 2 ROIC, regulators	Proton	MGH	Sept 2018	DD	SEFI, dark current
Spin 2 ROIC	Heavy ion	TAMU	Sept 2018	SEE	Latch-up, SEFI

6.2.2 Heavy Ion Tests (TAMU April 2016)

In this initial round of heavy ion testing of the Spin 0 ROIC, the DUT was evaluated for single event latch-up and SEE susceptibility. See below for a summary of tests:

- **Latch-up Testing**
  - **Heat DFPA to 40C**
  - **Integrate 1ms (count up) / pulse gates on**
  - **Monitor/Record Current During Entire Exposure**
  - **Capture Video Frames During Entire Exposure**
  - ✓ **No latchup or other destructive SEE were observed to the highest level tested : Linear Energy Transfer (LET)≤110 MeV·cm2/mg, 40°C**
- **SEE Testing**
  - **DFPA at Ambient Temp**
  - **Write stripe pattern to NUC**
  - **Integrate 1ms (count up) / pulse gates off**
  - **Monitor/Record Current During Entire Exposure**
  - **Capture Video Frames During Entire Exposure**
  - ✓ **Non-destructive SEE were observed during the testing. These events were observed at each LET tested from 33 to 78 MeV·cm2/mg at ambient temperature**

Heavy ion testing took place at the radiation test facility at Texas A&M University (TAMU). This facility runs 24 hours a day and time must be reserved well in advance. To facilitate our testing, we used Radiation Test Solutions (RTS) out of Colorado Springs, CO. RTS reserves multiple blocks of time for their client's testing and often have availability when TAMU is booked. RTS provides a test consultant who interfaces with the TAMU beam operators, and provides test recommendations based on results to use beam time most efficiently.

Five beam types were chosen for testing to span the desired LET range as seen in Figure 19. See Figure 20 for flow chart and beam table for the test protocol.

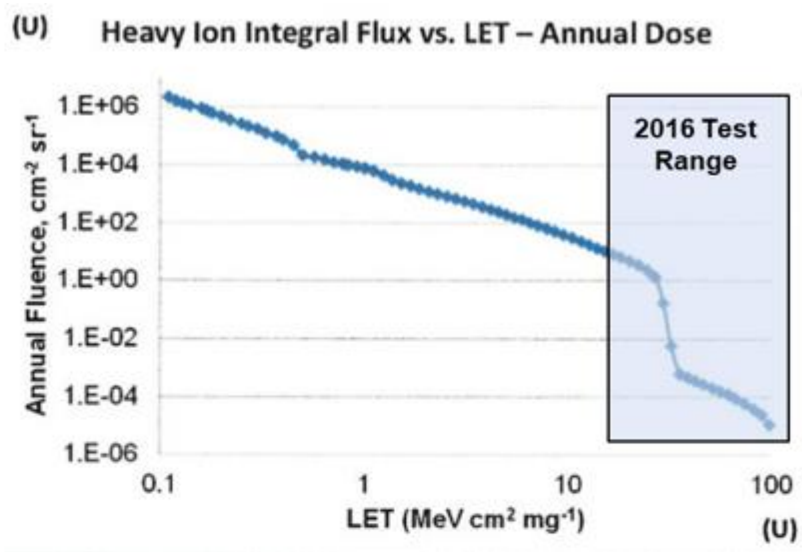

Figure 19. 2016 LET Test Range.

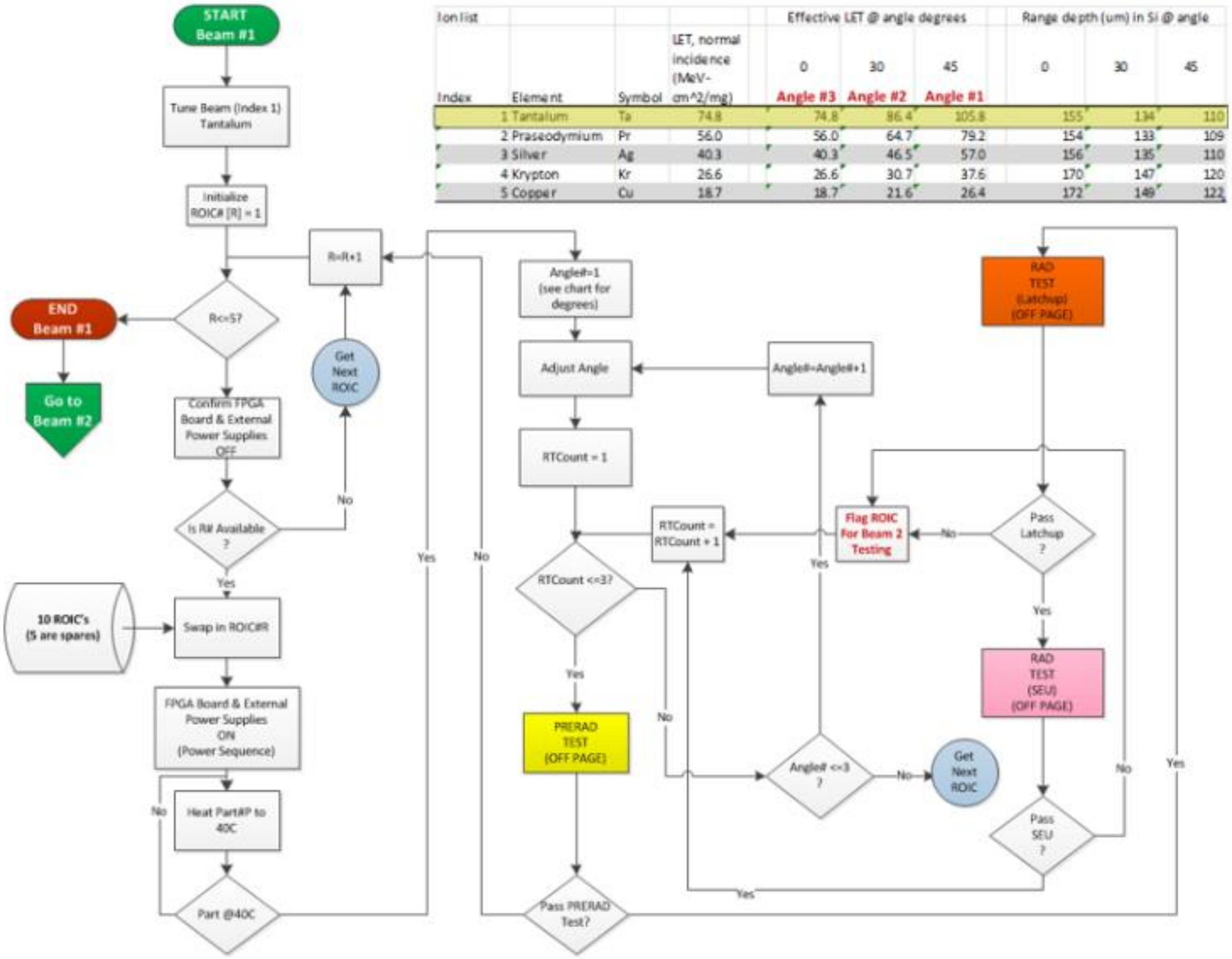

Ion list				Effective LET @ angle degrees			Range depth (um) in Si @ angle		
Index	Element	Symbol	LET, normal incidence (MeV-cm^2/mg)	0 Angle #3	30 Angle #2	45 Angle #1	0	30	45
1	Tantalum	Ta	74.8	74.8	86.4	105.8	155	134	110
2	Praseodymium	Pr	56.0	56.0	64.7	79.2	154	133	109
3	Silver	Ag	40.3	40.3	46.5	57.0	156	135	110
4	Krypton	Kr	26.6	26.6	30.7	37.6	170	147	120
5	Copper	Cu	18.7	18.7	21.6	26.4	172	149	122

Figure 20. Selected beams and test protocol.

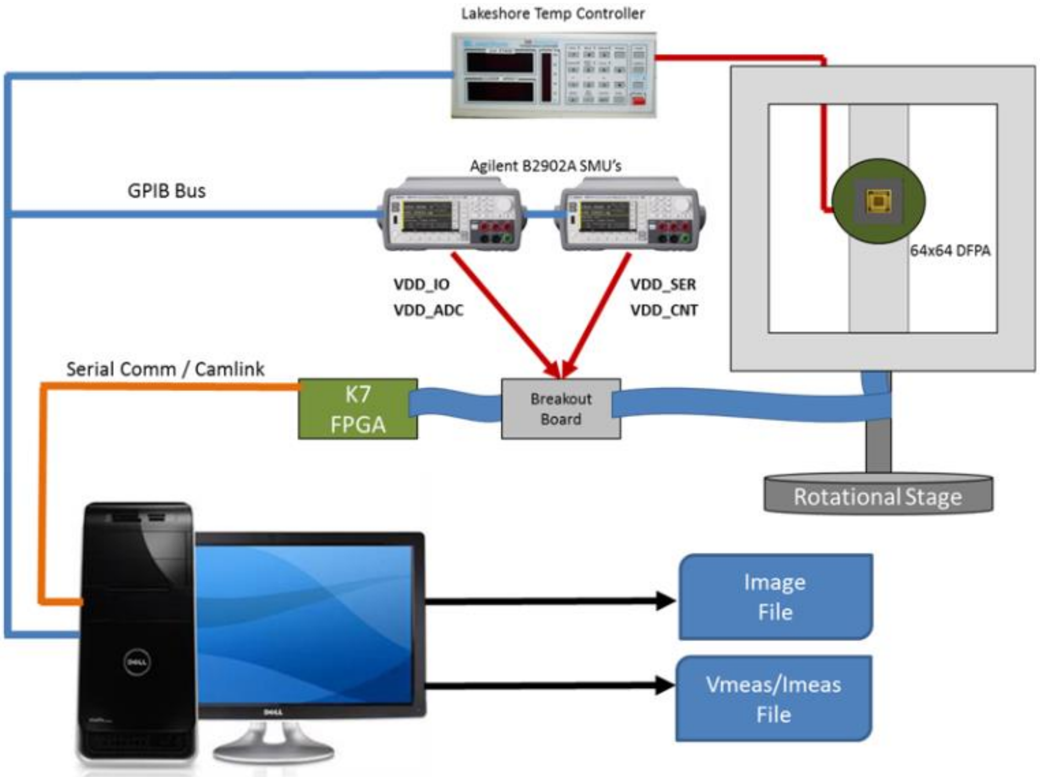

Figure 21. Test block diagram.

Since the TAMU radiation test facility runs 24/7, we prepared as much as possible outside of the beam time. The night before our beam time, we arranged our test setup on a mobile cart (see Figure 22). Once our beam time began, we relocated the test setup to the radiation cave using the cave elevator (also Figure 22). Once in the cave, we positioned the DUT on the stage in front of the beam (see Figure 23). Our RTS consultant, John Bird, then fine-tuned the placement of the DUT in front of the beam (also Figure 23).

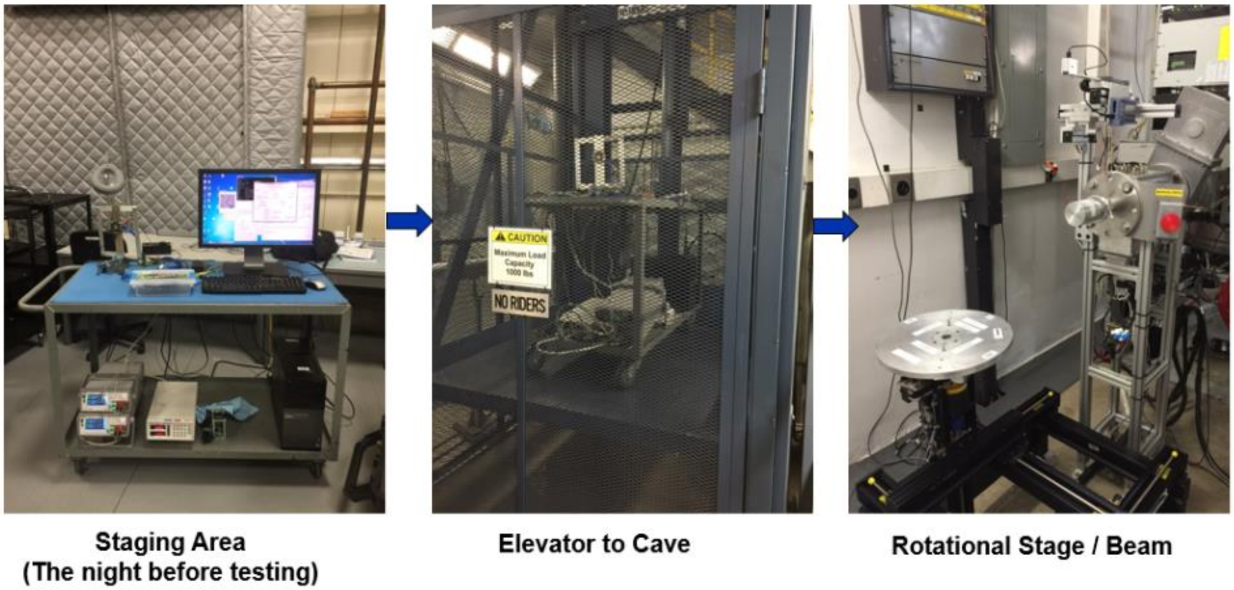

Figure 22. Test setup at TAMU.

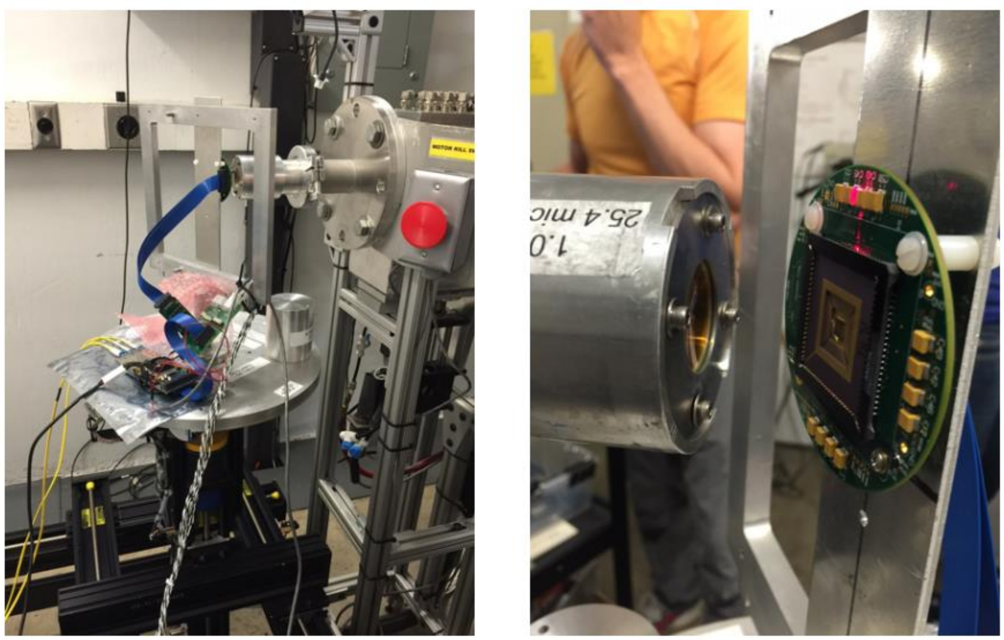

Figure 23. Alignment of DUT with beam.

Results show no SEL (single event latch-up) up to max tested LET of 110 MeV-cm^2/mg. However, many instances of SEFI were observed at each LET (33-78 MeV cm2/mg) resulting in bad pixels, columns, etc. (see Figure 24). All functional interrupts could be repaired by power cycling the device. This data was promising considering the Spin 0 ROIC was not designed with any radiation hardness in mind. This round of testing suggested that design improvements to remove static memory from the ROIC would mitigate instances of SEFI (see 6.2.5).

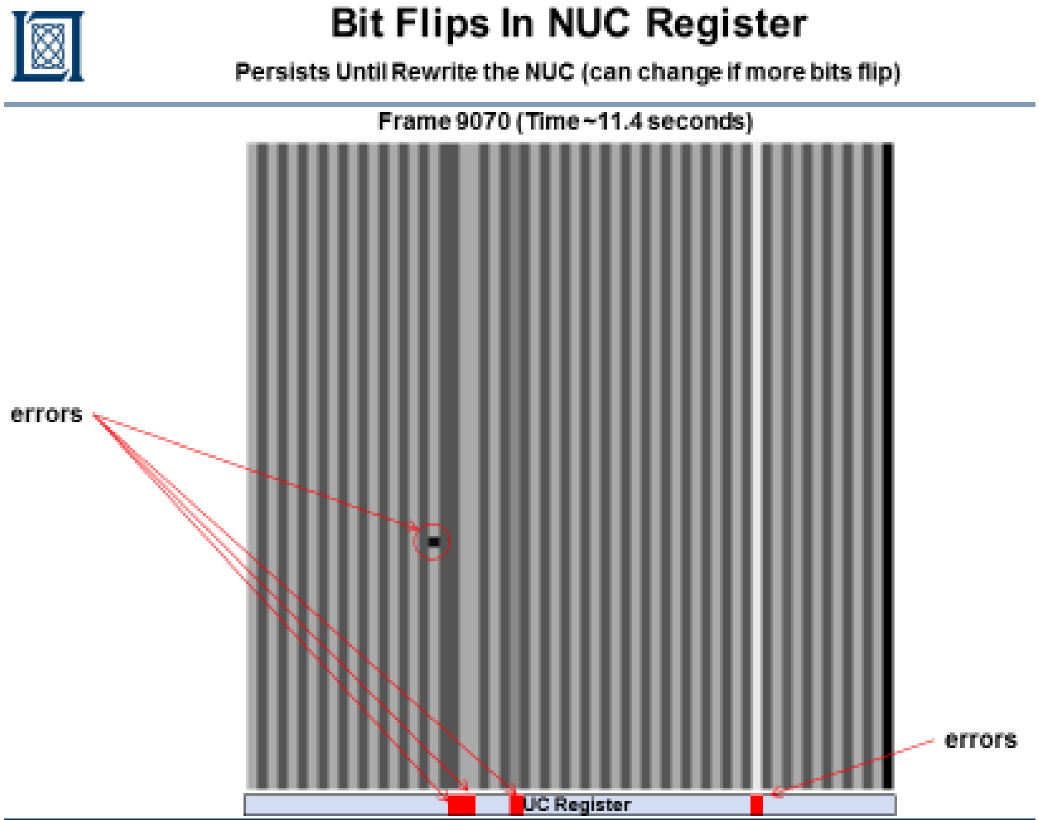

Figure 24. Heavy ion tests 2016 - SEFI bit flips.

6.2.3 Proton Tests (MGH June 2016)

In this initial round of proton testing, three hybrids and three ROICs from Spin 0 were evaluated at 70 and 160 MeV beam energy. At each energy level, the DUT was exposed three times to hit 1x, 3x, and 9x margins. See Table 10 for more detail. Figure 25 shows the experimental setup at Massachusetts General Hospital in the Francis H Burr Proton Beam Therapy Center.

Table 10. MGH 2016 Test Matrix

MGH proton test matrix	CM01	R07	CM06	R08	CM10	R09	
							Comments
Energy, MeV	70	70	70	70	160	160	Beam parameters
Flux, p+/cm2/s	1.90E+07	1.90E+07	1.90E+07	1.90E+07	3.80E+06	3.80E+06	
Exposure1,sec	40.00	40.00	40.00	40.00	40.00	40.00	*1st exposure*
Cumulative Fluence1, p+/cm2	7.60E+08	7.60E+08	7.60E+08	7.60E+08	7.60E+08	7.60E+08	1x margin
Exposure2,sec	80.00	80.00	80.00	80.00	80.00	80.00	*2nd exposure*
Cumulative Fluence2, p+/cm2	2.28E+09	2.28E+09	2.28E+09	2.28E+09	1.06E+09	1.06E+09	3x margin
Exposure3,sec	240.00	240.00	240.00	240.00	240.00	240.00	*3rd exposure*
Cumulative Fluence3, p+/cm2	6.84E+09	6.84E+09	6.84E+09	6.84E+09	1.98E+09	1.98E+09	9x margin
Modeled fluence, worst week solar, #p+	2.80E+07	2.80E+07	2.80E+07	2.80E+07	5.60E+06	5.60E+06	
Modeled fluence, 5yr mission, #p+	2.50E+07	2.50E+07	2.50E+07	2.50E+07	2.50E+07	2.50E+07	
FPA area, cm2	0.037						

Figure 25. Test setup at the MGH Francis H. Burr Proton Beam Therapy Center.

In the hybrids, it was found that dark current increased after each round of irradiation. However, the ROICs did not show any quantifiable change between the pre- and post-radiation data. Figure 26 and Figure 27 show an example of data from a single hybrid (CM01). While the data taken immediately after irradiation shows increased dark counts, it appears that some pixels self-anneal in the days after irradiation (see Figure 27).

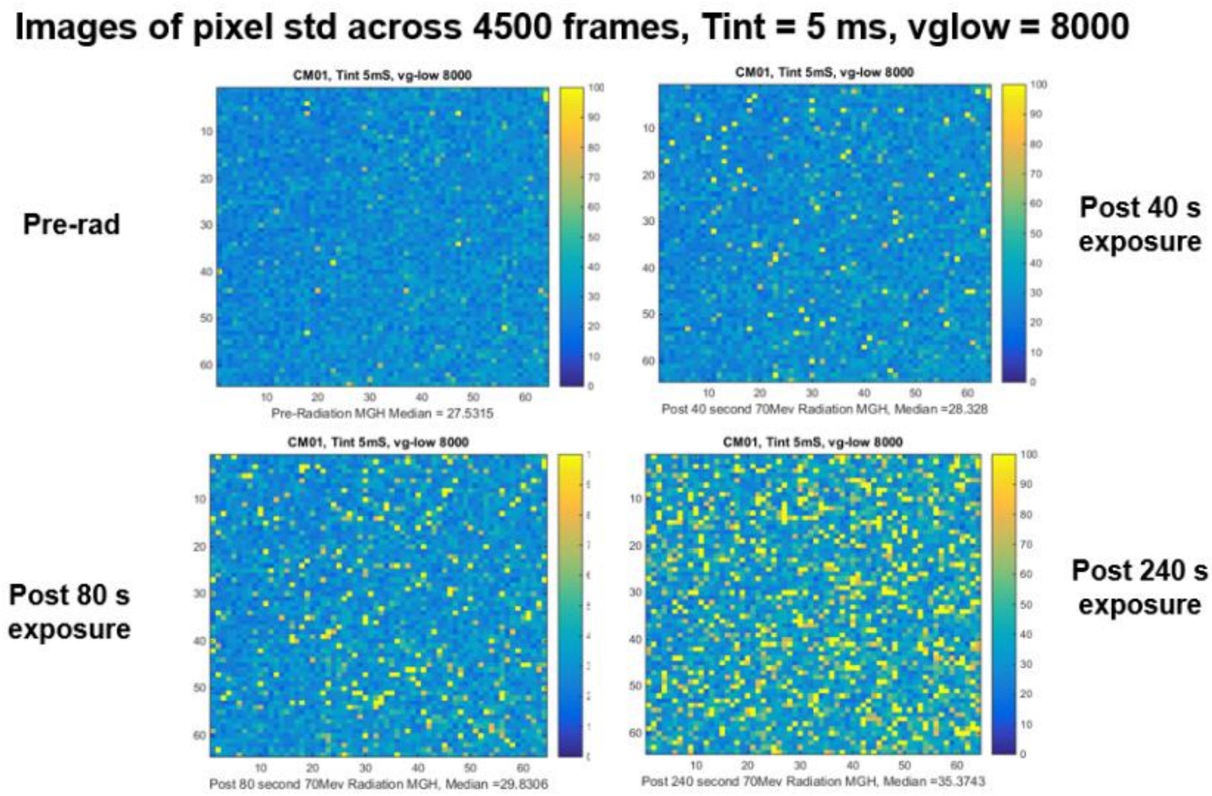

Figure 26. Pixel standard deviation for hybrid CM01 at the pre-radiation test and after each level of irradiation for the 70MeV beam energy, high gain.

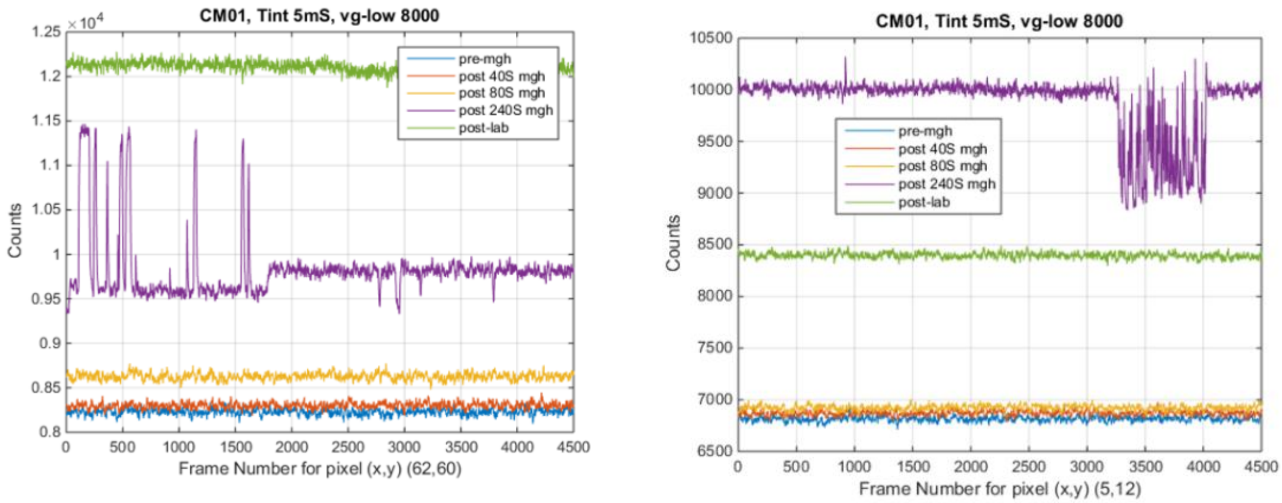

Figure 27. Dark counts per pixel over 4500 frames for hybrid CM01 at the pre-radiation test and after each level of irradiation for the 70 MeV beam energy, high gain. "Post-lab" means the data was taken several days after the radiation testing at MIT LL.

6.2.4 Gamma Tests (UML Aug 2016)

In this initial round of gamma testing, three ROICs and three hybrids from Spin 0 were tested. Two ROICs and two hybrids were tested in small increments up to 25 kRad total dose. The third ROIC and hybrid were tested in increments from 25 kRad to 500–700 kRad total dose. See Table 11 for a test outline.

Table 11. Gamma Test Outline (UML August 2016)

ROICs:
- **R10 (backup)**
- **R11**
- **R12**
- **R13**

HYBRIDS:
- **CMI5**
- **CMI7**
- **CMI8**
- **CMI9 (backup)**

Total Dose (krad)	R11	R12	R13	CMI05	CMI07	CMI08
Pre Rad	x	x	x	x	x	x
5	x	x		x	x	
15	x	x		x	x	
25	x	x	x	x	x	x
100			x			x
200			x			x
300			x			x
400			x			x
500			x			x
700						x

The DUT was biased during irradiation and test data was acquired before and after each level of irradiation.

In the ROICs, increased leakage counts with higher total dose were observed (Figure 28). However, in the hybrids, decreased counts with minimal increase in temporal noise were observed (Figure 29). Quantum efficiency before and after irradiation was measured and it was found that although ROIC leakage increased with total dose, detector QE fell (see Table 12).

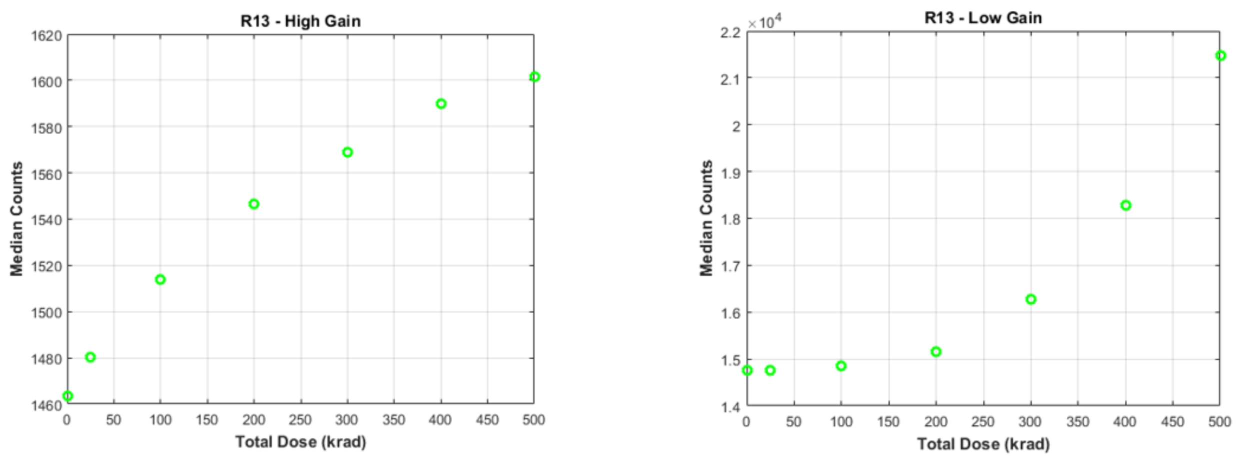

Figure 28. ROIC median counts increased with total dose, high and low gain.

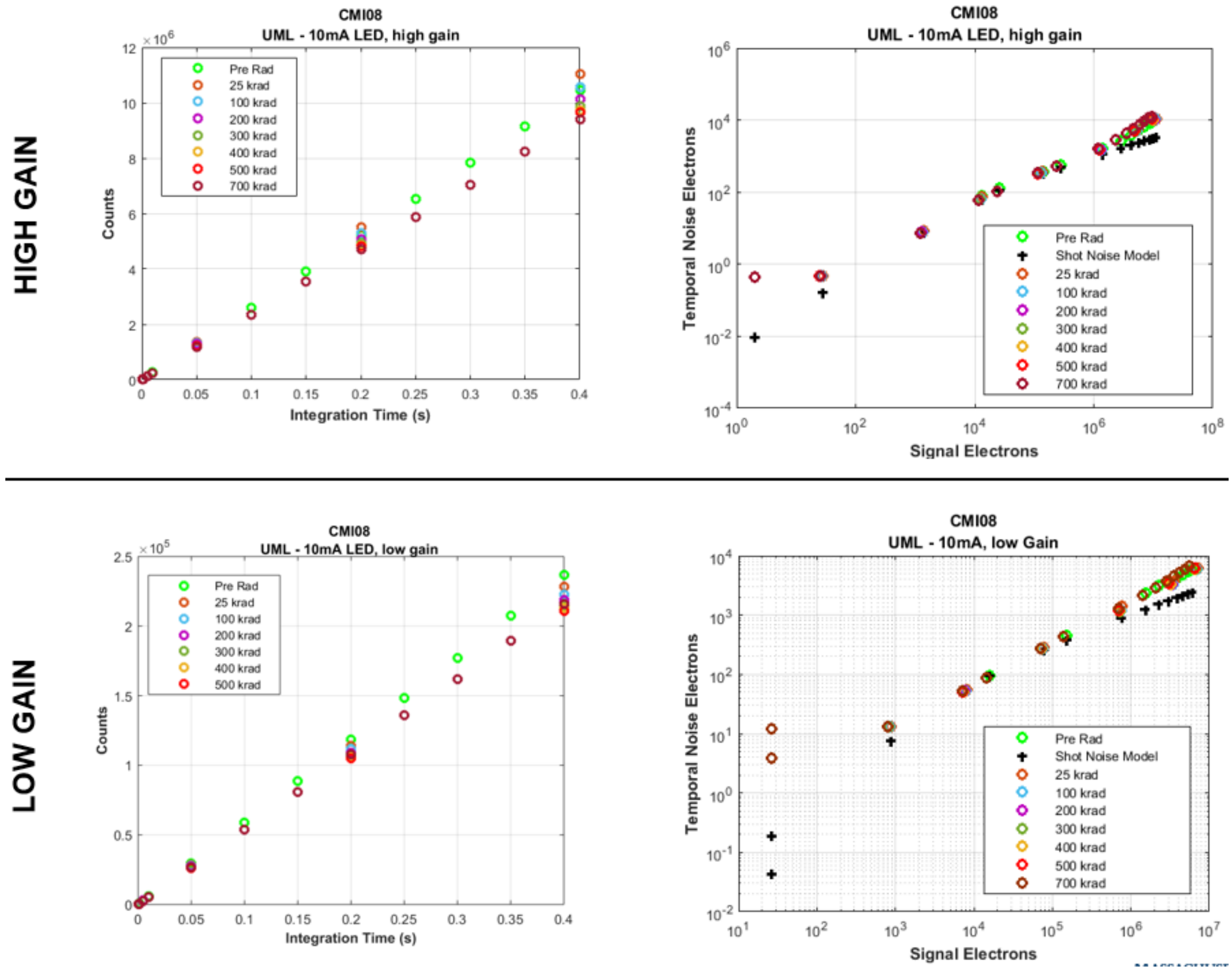

Figure 29. Hybrid counts and noise vs. signal after each dose for high and low gain.

Table 12. Hybrid Detector QE Drop after 700 kRad Total Dose

- ~15% drop in QE after 700 kRAD total dose
- No observable drop in QE after 25 kRAD total dose

Total Dose	Device	QE (Low Gain)	QE (High Gain)
No RAD	CMI 02	80%*	80%*
No RAD	CMI 11	90%	90%
25 kRAD	CMI 07**	90%	90%
700 kRAD	CMI 08**	74%	74%

CMI 02 QE measured on slightly different setup, ~10% error expected in QE measurement
****Devices irradiated at UML***

6.2.5 Heavy Ion Tests (TAMU May 2017)

After redesigning the ROIC to eliminate static registers in the periphery, the Spin 1 ROICs were tested in 2017 with an expanded LET test range, which spanned from 2.7 to 110.6 MeVcm2/mg (see Figure 30). Tantalum, Silver, Krypton, Neon, and Argon beams were used to achieve these LETs. Four ROICs and two LT3021 voltage regulators were tested. No latch-up or destructive SEE were observed up to 110 MeV cm2/mg. Persistent SEE were no longer observed after the removal of the registers.

Since the static memory on the periphery of the chip was removed for radiation hardness in the Spin 1 design, it was not possible to write a stripe pattern to the array as was done in the Spin 0 testing. Instead, the pulse gates were disabled, causing each pixel to read zero counts unless affected by an SEU. Example upset data that only persisted for a single frame is shown in Figure 31.

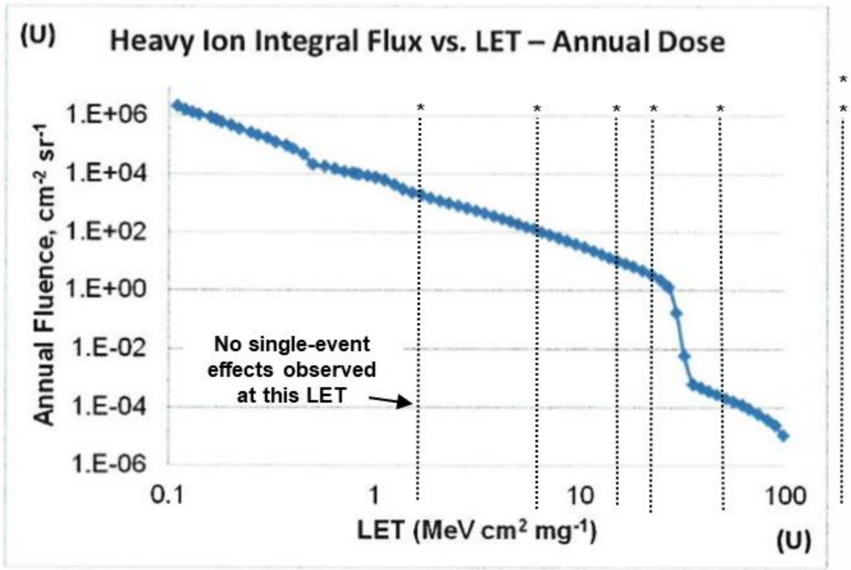

Figure 30. LET levels selected for this round of radiation testing (TAMU May 2017).

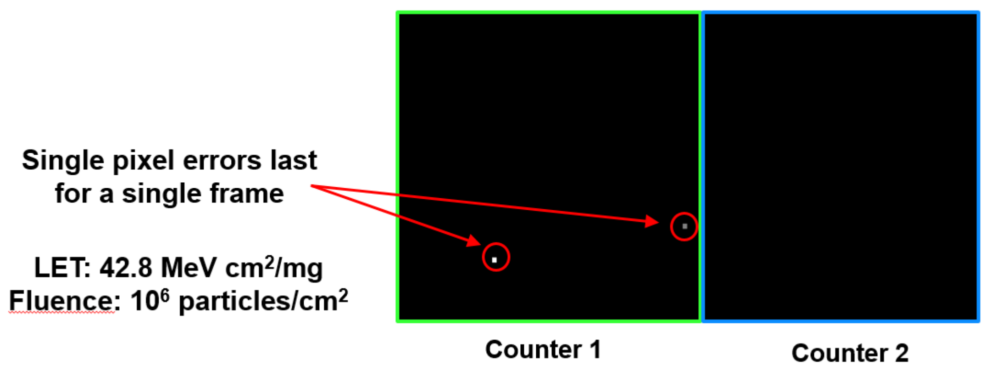

Figure 31. This image shows the single pixel errors that were observed during irradiation. These effects were not persistent and only appeared for one frame before being resolved.

Voltage regulators were also tested as depicted in Figure 32. Before, during, and after irradiation, the source and load current and voltage were monitored at 1ms intervals, with ~5000 data points collected. As seen in Table 13, measured transients were less than 10mV across the range of LETs. Table 13 gives specifics of those measurements during the irradiation period. At this level, there is no expected impact to device performance from heavy ion impact.

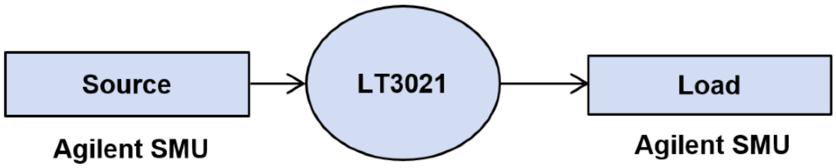

Figure 32. Voltage regulator test block diagram.

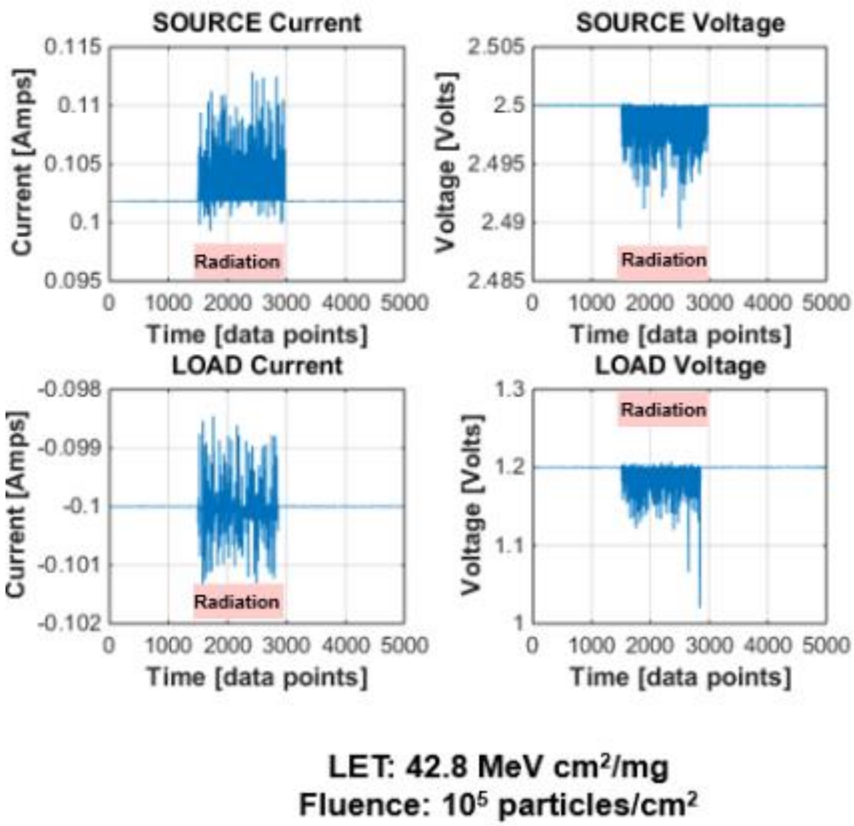

Figure 33. Voltage regulator results.

Table 13. Voltage Regulator Readings During Irradiation Period

	Max	Min	Mean	Median	Std
V Source [V]	2.50025	2.48945	2.49967	2.50000	0.00092
V Load [V]	1.20755	1.02051	1.19742	1.20036	0.00999
I Source [A]	0.11286	0.09929	0.10229	0.10184	0.00126
I Load [A]	-0.0985	-0.1014	-0.1000	-0.1000	0.00013

6.2.6 Proton Tests (MGH June 2017)

The second round of proton testing focused on the Spin 1 ROIC variants and hybrids. Eight total devices covering two designs (A5 and B5) were tested – two A5 hybrids, two B5 hybrids, two A5 ROICs, and two B5 ROICs. As in the previous year's test for the Spin 0 design, beam energies of 70 and 160 MeV were used with three exposures at each beam energy per part. The total dose after the six exposures for each part was about 1.5 kRad. As before, no effects were observed in the ROIC but some transient effects were observed in the hybrids.

Figure 34 shows frame 2187 in run 3 of the 70 MeV beam for hybrid A503. These effects did not persist from frame to frame, similar to the results of the Spin 0 design when tested in 2016, and were observed in both the A5 and B5 designs.

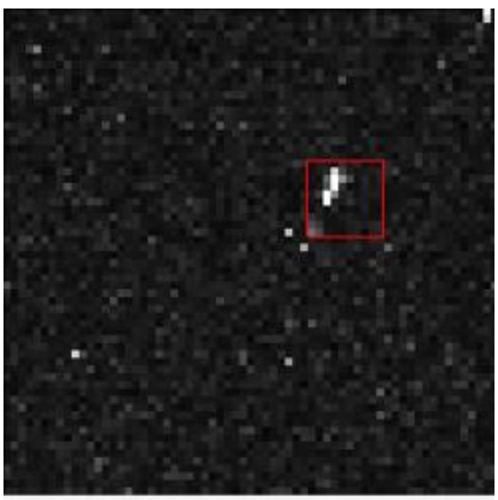

Figure 34. An example of single event effects observed during proton irradiation.

Impact on dark current in the detectors:

Displacement damage (proton) testing was found to produce a small increase in measured median dark current (up to 12%), for the maximum proton dose equivalent to 10 kRad. In addition to an increase in the median dark current (Figure 36), each photodiode array exhibits an increase in the number of pixels with dark currents significantly above the median, forming a tail of high dark current pixels in the distribution. These pixels with much higher dark current occur randomly distributed spatially across the arrays, as shown in the right side of Figure 35. This is consistent with past proton testing on InGaAs/InP photodiodes at MIT LL and is understood to be a result of the various types of displacement damage that occur in the semiconductor. Single primary displaced atoms tend to form isolated vacancy and interstitial defects that lead to smaller increases in dark current compared to displacement damage events that produce extended chains of displaced atoms. See, for example, **Error! Reference source not found.** below (D. Tang, 2016). Past proton testing on similar InGaAs devices has shown dark current increases of >10x at this DD dose level, however that testing was sensitive to lower levels of dark current than in this testing (sub-fA) (J. E. Hubbs, 2010).

Based on measurements at the manufacturer of the InGaAs arrays, median pixel dark currents were ~45fA at 20°C. Since this is significantly below the measured on-ROIC dark current before radiation exposure, it is likely that the actual increase in dark current is greater than the measured increase for arrays on ROICs after exposure. In other words, DFPA dark current is not the driving factor of noise.

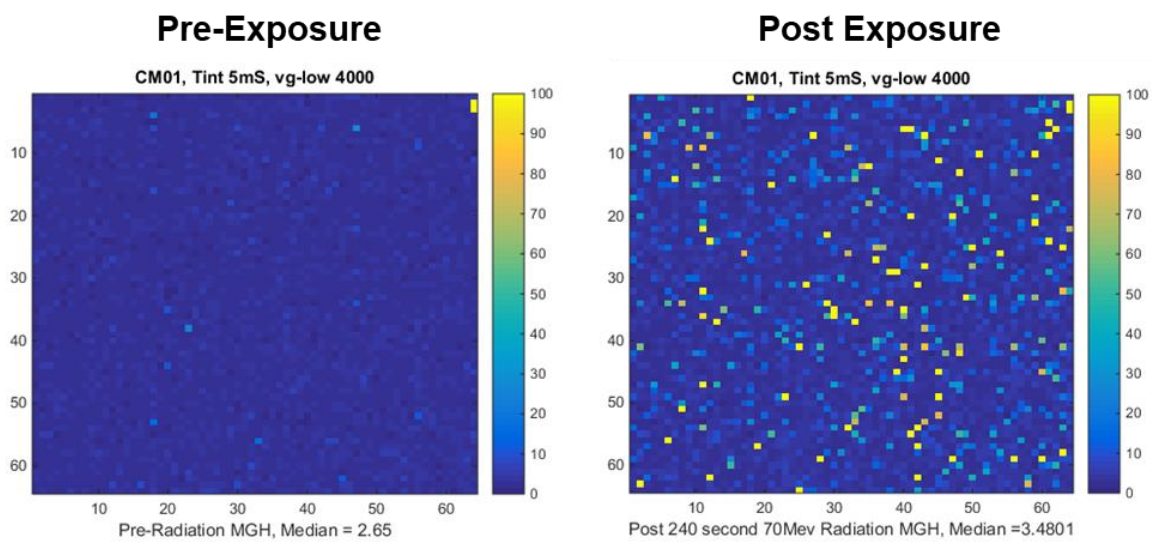

Figure 35. Maps of dark current in an InGaAs DFPA hybrid before and after proton exposure. Pixels with high dark current after exposure likely caused by extended cascade of displaced atoms.

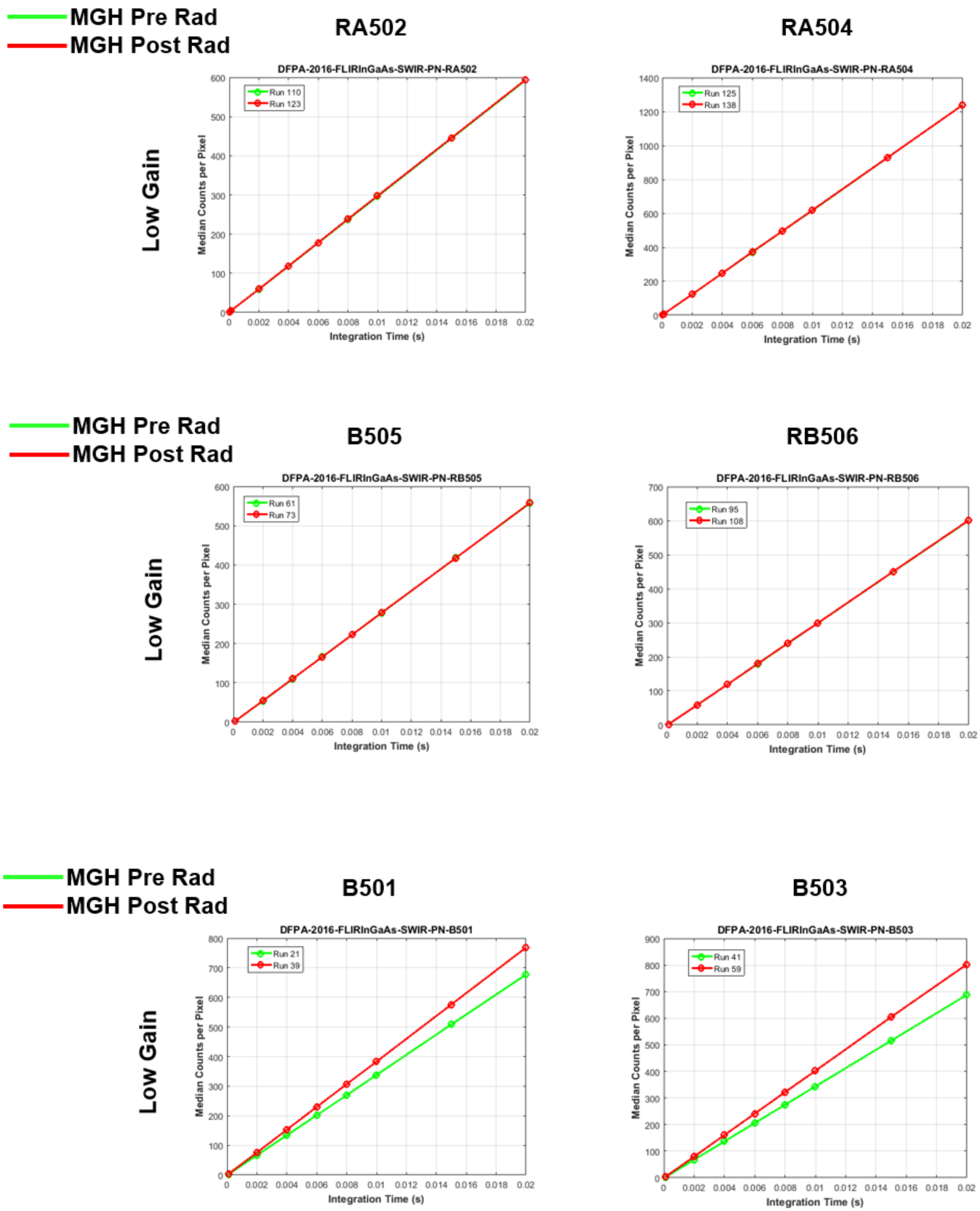

Figure 36. Median dark counts per pixel pre (green) and post (red) radiation for hybrids. Some curves of pre and post data exactly overlap, indicating no change from irradiation.

Quantum Efficiency:

Experimentally a small (<5%) reduction in QE was measured after proton exposure (Figure 37). This is roughly consistent with past testing of similar InGaAs photodiodes discussed in published results (J. E. Hubbs, 2010).

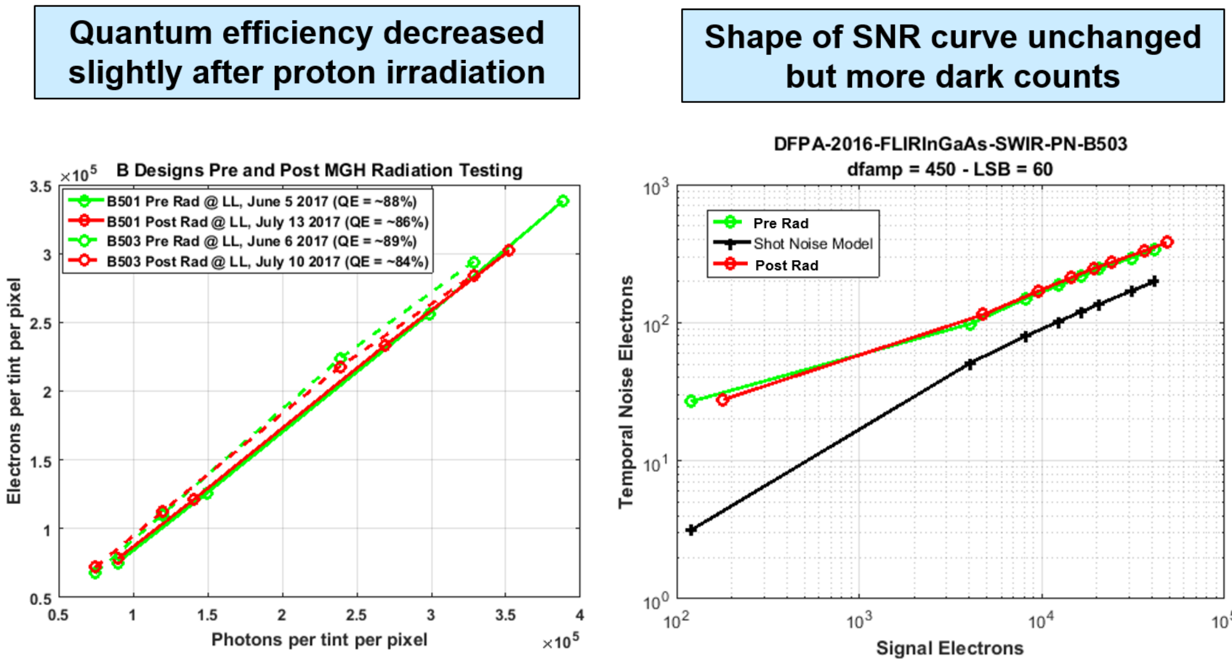

Figure 37. Quantum efficiency and signal-temporal noise curves for hybrids.

6.2.7 Gamma Tests (UML Aug 2017)

In this Spin 1 Gamma testing round, one B5 ROIC, two B5 hybrids, and three LT3021 voltage regulators were tested up to 1 MRad (see Figure 38).

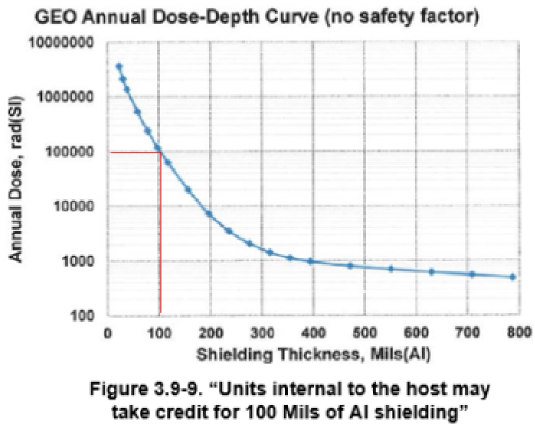

Original Radiation Environment

Year	Dose	2x
1	25 krad	50 krad
2	50 krad	100 krad
3	75 krad	150 krad
4	100 krad	200 krad
5	125 krad	250 krad

Alternate Radiation Environment

Year	Dose	2x
1	100 krad	200 krad
2	200 krad	400 krad
3	300 krad	600 krad
4	400 krad	800 krad
5	500 krad	1 Mrad

Figure 38. Radiation environment specifications and shielding thickness required.

Similar effects were observed to the previous year's tests, where the ROIC saw increased leakage counts while the detector suffered loss in QE with higher total dose. The left plot in Figure 39 shows increased dark current with total dose. The plot on the right shows an initial dip in median counts and then an increase as total dose increases. It is believed that although the QE of the detector dips, the increased leakage current in the ROIC eventually dominates. In addition, at total doses beyond 500 kRad, an additional effect, such as a threshold shift, could be causing the increase in counts observed and should be investigated in future testing.

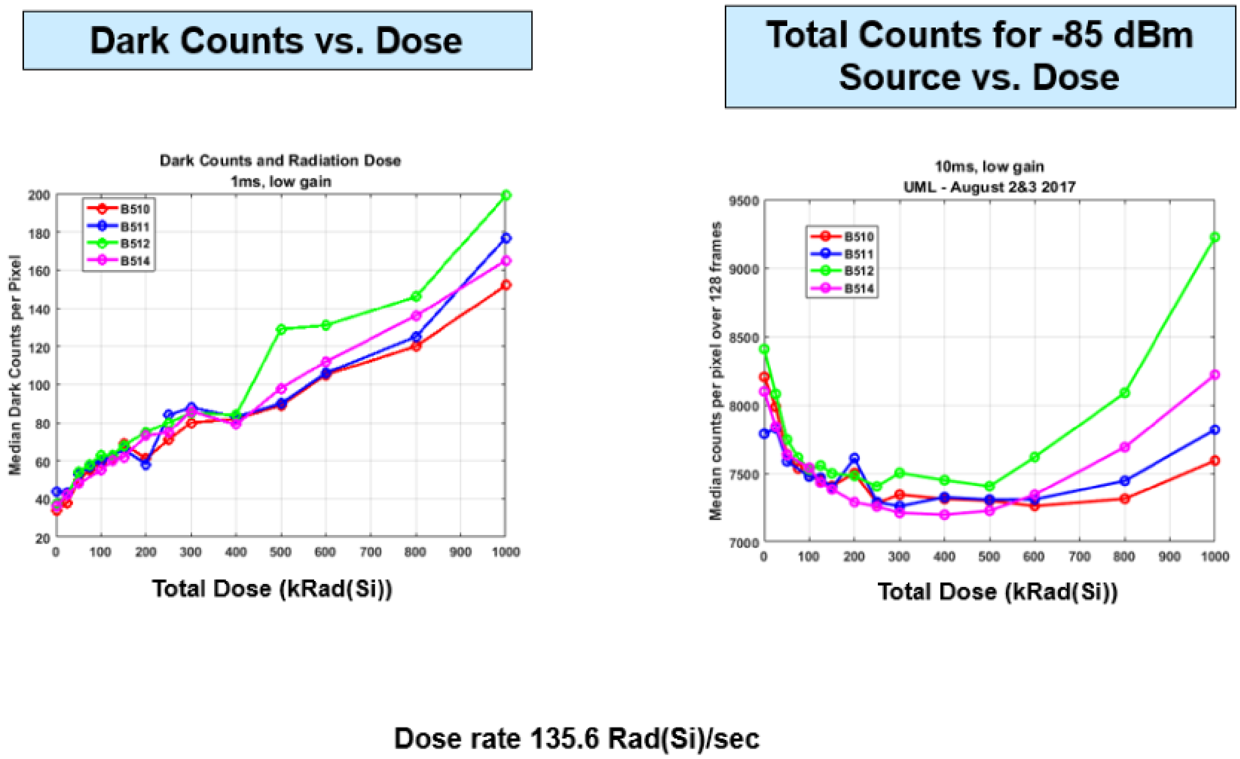

Figure 39. Dark counts and signal counts as a function of total dose.

In the left plot in Figure 40, a decrease in QE can be observed for four B5 hybrids before irradiation and post irradiation. An increase in temporal noise can also be observed in the plot on the right.

Quantum efficiency impact due to detectors:

Experimentally it was found that ionizing radiation at lower total doses (<50 kRad gamma exposure) had little or no impact on QE in the devices, while at higher doses (up to 1Mrad) the QE was reduced by up to 17% (Figure 37Figure 39). In some cases, the QE reduction was also accompanied by an apparent shift in the bias voltage dependence of the QE, indicating a change in the electric field conditions may be present in the photodiode due to the exposure. Under the maximum 1 MRad TID exposure, application of a higher bias could not recover the loss in QE. This is one indication that these high doses also cause a reduction in carrier lifetime.

Experimentally, it was found that ionizing radiation increased dark current roughly proportional to the dose. With the final 1 MRad TID, dark current appeared to increase by up to 400%, as shown in Figure 39, where dark count increases with dose from ~40counts before irradiation to approximately 160counts after 1000kRad dose.

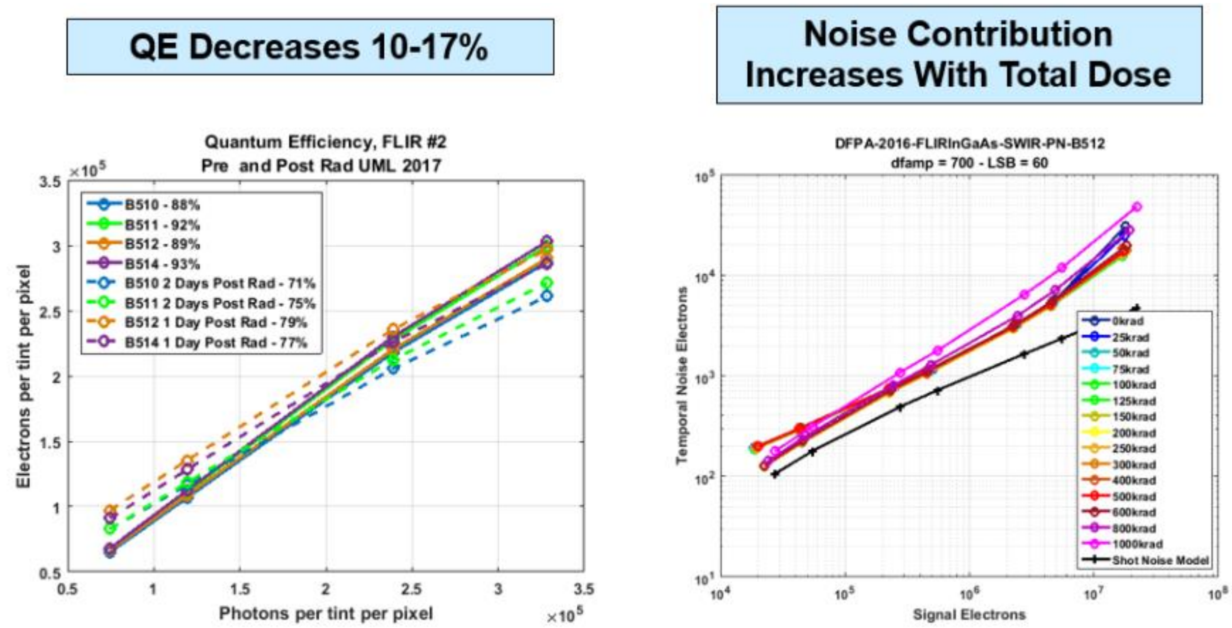

Figure 40. Quantum efficiency and signal-noise over course of radiation exposure.

The voltage regulators were also gamma irradiated in August 2017. After gamma irradiation, the voltage regulators failed to hold regulation over the load range and the output voltage changed value, as seen in Figure 41. In two of the three DUTs, the regulator failed to function correctly after 25 kRad total dose. One of the regulators (regulator 2) failed to function in the pre-radiation test.

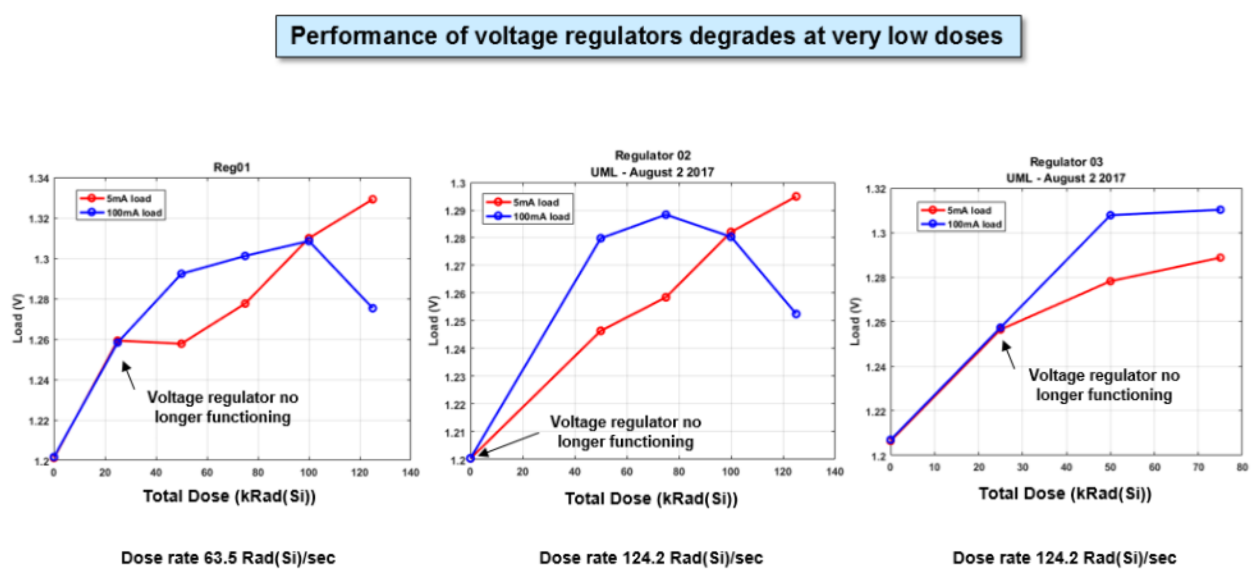

Figure 41. Voltage regulator performance as a function of total dose.

6.2.8 Proton Tests (MGH September 2018)

The third and final round of proton testing focused on the Spin 2 ROIC and voltage regulators. Three C2A ROICs and three regulators were tested. Each ROIC DUT was exposed to three beam energies (160, 70, and 50 MeV) with three exposures at each energy for a total dose around 1.7 kRad. All tests were performed at high and low gain. The regulators each had one exposure for a total dose of 10 kRad each. Due to time constraints, the regulators were not biased during exposure.

As seen in the Spin 1 testing, the Spin 2 ROICs did not exhibit any effects from frame to frame (as was seen in the detectors) due to proton irradiation. There was also no effect in leakage current between the pre-radiation data taken immediately before irradiation and the post-radiation data taken after all exposures. See Figure 42 for data on ROIC C2A04.

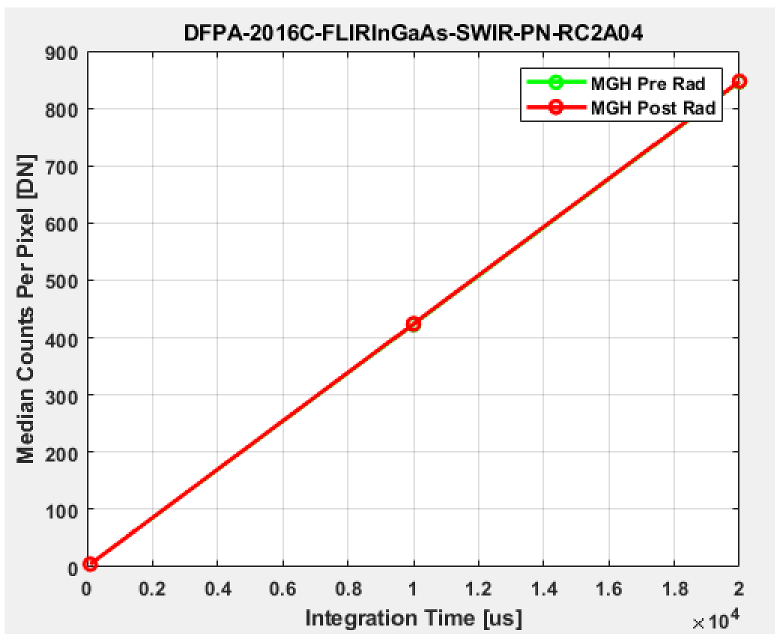

Figure 42. Leakage counts pre- and post-radiation.

Each of the three regulators were exposed to 10 kRad total dose. After this exposure, no adverse effect was observed (see Figure 43).

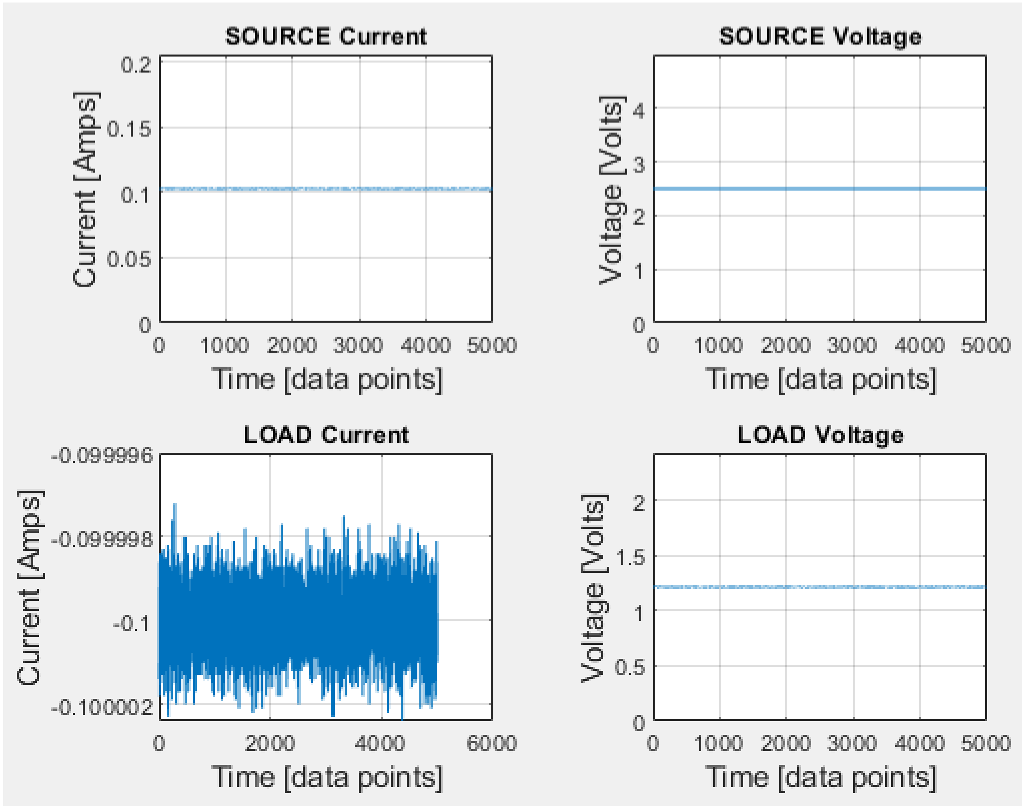

Figure 43. "Left" regulator after 10 kRad total dose.

In conclusion, the layout changes made between Spin 1 and Spin 2 did not affect the radiation hardness of the device in regards to gamma radiation.

6.2.9 Heavy Ion Tests (TAMU September 2018)

The third and final round of heavy ion testing focused on the Spin 2 ROIC. The purpose of the test was to determine if layout changes made between Spin 1 and Spin 2 would affect the radiation hardness of the ROIC. Three C2A ROICs were tested. As in the previous two years, latch-up was tested at the highest LET (Tantalum, 110.6 MeV*cm^2/mg) with the DUT heated to 40^{o}C. Latch-up was not observed on any of the three ROIC DUTs. The LET space was sampled from 2.7–110.6 MeV*cm^2/mg using Tantalum, Krypton, and Neon beams (see Table 13). While single event upsets were observed, there were no effects that persisted from frame to frame (see Figure 44). This is the same result observed in the Spin 1 heavy ion testing.

Table 13. Summary of the LET Space Captured over the Three Years of Heavy Ion Testing

LET Range [MeV*cm^2/mg]

2016 (Spin 0)	2017 (Spin 1)	2018 (Spin 2)
32.7	2.7	2.7
42.8	8.4	3.8
49.5	28.3	28.3
59.2	42.8	40.0
78.2	78.2	78.2
90.2	110.6	110.6
110.6		

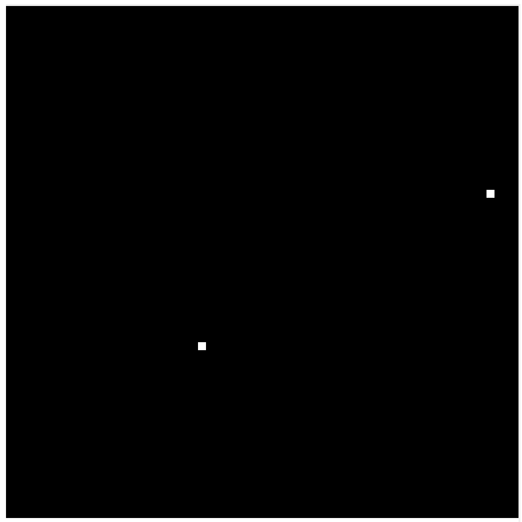

*Figure 44. ROIC C2A01 during run 3 (frame 736, 78 MeV*cm^2/mg, Tantalum). Two upsets can be observed (white pixels), but these errors do not persist to the next frame.*

In conclusion, it was found that the Spin 2 design exhibits the same tolerances as observed with the Spin 1 design. Both designs are immune to single event latch-up under the specified conditions and there are no persistent SEUs observed.

7. CONCLUSIONS

The initial designs for the ROIC, radiation tested during the first campaign, showed no susceptibility to single-event latch-up. However, there was significant and unacceptable functional failures due to hard-coded registers. These failures resulted in large-scale image structures, which had to be corrected.

A second, updated design removed the hard-coded registers and replaced them with programmable registers. Subsequent testing during the second test campaign showed, once again, no susceptibility to SEL. In addition, the functional failures were no longer present. Only expected single-event upsets on a frame-to-frame basis were present. Changes in dark current occurred, but at acceptable levels, meaning our algorithm performance was not impacted. Small changes in quantum efficiency were detected, also at acceptable levels. A third spin (Spin 2) kept the same changes as Spin 1, but incorporated some layout changes. Spin 2 performed the same as Spin 1 under the same radiation conditions, as expected.

In conclusion, the first and second spiral designs (Spin 1 and Spin 2) for the DTA ROIC are considered acceptable for flight use in the geosynchronous equatorial orbit environment for the specified mission.

This page intentionally left blank.

REFERENCES

Barde, S. (2000, Dec). Displacement Damage Effects in InGaAs Detectors:Experimental Results and Semi-Empirical Model Prediction. *IEEE TRANSACTIONS ON NUCLEAR SCIENCE*, pp. 2466-2472.

Belgian Institute for Space Aeronomy. (2019, Jan). Retrieved from SPENVIS: https://www.spenvis.oma.be/help/background/traprad/traprad.html

BISA (Belgian Institute for Space Aeronomy). (2019, January). Retrieved from SPENVIS: https://www.spenvis.oma.be

Gilard, O. (2018, March). Damage Factor for Radiation-Induced Dark Current in InGaAs Photodiodes. *IEEE TRANSACTIONS ON NUCLEAR SCIENCE*, pp. 884-895.

J. E. Hubbs, e. a. (2010). Radiometric and Radiation Characterization of InGaAs Focal Plane Arrays from Sensors Unlimited. *MSS Detectors.*

Roche, P. (2009). *SEE and TID Radiation Test Results on ST Circuits in 65nm CMOS Technologies.* Crolles, France: ST Microelectronics.

Vasilescu, A., & Lindstroem, G. (2000). *Displacement damage in silicon.* on-line compilation.

Tang, D., et.al. Time dependent modeling of single particle displacement damage in silicon devices. Microelectronics Reliability. Vol 60, May 2016, pp 25-32.

This page intentionally left blank.

GLOSSARY

Acronym	Definition
BOM	Bill of materials
DD	Displacement damage
DFPA	Digital focal plane array
NIEL	Non-ionizing energy loss
NUC	Non-uniformity correction
RHA	Radiation hardness assurance
ROIC	Read-out integrated circuit
SEE	Single-event effect
SEFI	Single-event functional interrupt
SEL	Single-event latch-up
SEU	Single-event upset
TID	Total ionizing dose

REPORT DOCUMENTATION PAGE

Form Approved
OMB No. 0704-0188

1. REPORT DATE *(DD-MM-YYYY)*	2. REPORT TYPE	3. DATES COVERED *(From - To)*
20-January-2021	Technical Report	

4. TITLE AND SUBTITLE

Digital Tracker Array Radiation Test Report

5a. CONTRACT NUMBER

FA8702-15-D-0001

5b. GRANT NUMBER

5c. PROGRAM ELEMENT NUMBER

6. AUTHOR(S)

David Fischi, Suzannah Riccardi, Jim Wey, Anthony Kryzak, Thomas Gardner, Alex McIntosh, Sandra Lee, Megan Blackwell

5d. PROJECT NUMBER

5e. TASK NUMBER

5f. WORK UNIT NUMBER

7. PERFORMING ORGANIZATION NAME(S) AND ADDRESS(ES)

Lincoln Laboratory, MIT
244 Wood Street
Lexington, MA 02421-6426

8. PERFORMING ORGANIZATION REPORT NUMBER

TR-1245

9. SPONSORING/MONITORING AGENCY NAME(S) AND ADDRESS(ES)

Gary Tutungian
AFLCMC/AZS
20 Schilling Circle
Hanscom AFB MA 01731

10. SPONSOR/MONITOR'S ACRONYM(S)

AFLCMC/AZS

11. SPONSOR/MONITOR'S REPORT NUMBER(S)

12. DISTRIBUTION/AVAILABILITY STATEMENT

Distribution Statement A

13. SUPPLEMENTARY NOTES

None

14. ABSTRACT

For the Digital Tracker Array (DTA) program, there were some unique concerns and constraints, which needed to be addressed. The primary component of this design was a hybrid sensor based on the Massachusetts Institute of Technology Lincoln Laboratory (MIT LL) Digital-pixel Focal Plane Array (DFPA) which was bump-bonded to InGaAs short wave band infrared detectors. Though used successfully in ground experiments, its space capability was an open question. In particular, the CMOS-based design and its susceptibility to radiation was unknown. Further, because the design of the package was extremely size, weight, and power constrained, radiation mitigation could become a problem (BISA, Belgian Institute for Space Aeronomy, 2019).

15. SUBJECT TERMS

16. SECURITY CLASSIFICATION OF:			17. LIMITATION OF ABSTRACT	18. NUMBER OF PAGES	19a. NAME OF RESPONSIBLE PERSON
a. REPORT	b. ABSTRACT	c. THIS PAGE			
Unclassified	Unclassified	Unclassified	Unclassified	72	19b. TELEPHONE NUMBER *(Include area code)*